Distinct basin-scale-distributions of aluminum, manganese, cobalt, and lead in the North Pacific Ocean

Linjie Zheng [a], Tomoharu Minami [a,b], Wataru Konagaya [a], Cheuk-Yin Chan [a], Makoto Tsujisaka [a], Shotaro Takano [a], Kazuhiro Norisuye [c], and Yoshiki Sohrin [a,*]

[a] Institute for Chemical Research, Kyoto University, Gokasho, Uji, Kyoto 611-0011, Japan

[b] Institute of Science and Engineering, Kanazawa University, Kakuma, Kanazawa, Ishikawa 920-1192, Japan

[c] Faculty of Science, Niigata University, Ikarashi-2-cho, Nishi-ku, Niigata 950-2181, Japan

*Corresponding author: Y. Sohrin. E-mail address: sohrin@scl.kyoto-u.ac.jp

Abstract

Aluminum (Al), manganese (Mn), cobalt (Co), and lead (Pb) are key trace elements in seawater and thus significant in chemical oceanography research. However, although all of these elements are highly scavenged in the ocean, only a few studies focus on the intercomparison of their distributions. Here, we report the basin-scale and full-depth sectional distributions of these elements observed during three GEOTRACES Japan cruises in the North Pacific. We confirmed that a surface maximum of the dissolved (d) species is not a common feature for the four elements and that the d species have the lowest concentrations in the Pacific Deep Water (PDW) as compared to other oceans. The elements showed different speciations and distributions. The fraction of labile particulate (lp) species was calculated as the difference between the total dissolvable (td) species and d species. The lpM/tdM ratio, where M refers to an element, is highest for Al, at 0.66 ± 0.31 (average ± sd, n = 489), and lowest for Pb, at 0.02 ± 0.08 (n = 575). Further, the distribution of each element is uniquely related to ocean circulation. The tdAl concentration is high in the Equatorial Under Current (EUC), the North Equatorial Current (NEC), and the Lower Circumpolar Deep Water

(LCDW). Manganese is supplied from reductive sources such as sediments on the continental shelves around the northern boundary. Cobalt is concentrated in the North Pacific Intermediate Water (NPIW) and in the Equatorial Pacific Intermediate Water (EqPIW) owing to the combined effects of supply from the continental shelves, biogeochemical cycling, and scavenging. Lead shows a subsurface maximum centered at ~35°N and ~200 m depth, implying an association with the formation of the Subtropical Mode Water (SMW) and the Central Mode Water (CMW). Although the subsurface Pb maximum in the Atlantic has diminished over the last three decades owing to the ban on leaded gasoline use, it has been sustained in the North Pacific through the growth of other anthropogenic sources in Asia and Russia. We propose that the enrichment factor of dM, defined as EF(dM) = $(dM/dAl)_{seawater}/(M/Al)_{upper\ crust}$, where $(M/Al)_{upper\ crust}$ is the molar ratio in upper crustal abundance, can be a good parameter for the sources. The median is 1.3×10^2 (n = 436) for EF(dMn), 3.2×10^2 (n = 430) for EF(dCo), and 1.2×10^3 (n = 413) for EF(dPb). The EF(dPb) found in this study is on the same order of magnitude as the EF values for aerosols found in the literature, suggesting that the deposition of aerosols is a major source for dPb. Because EF(dMn) and EF(dCo) are ten to hundred times higher than the EF for aerosols, sources other than the aerosol deposition are more significant contributors to the concentrations of Mn and Co.

Keywords: GEOTRACES; Trace metals; Ocean sections; Scavenging; Biogeochemical cycling; Anthropogenic pollution

1. INTRODUCTION

Elements in seawater have been divided into conservative, nutrient (or recycled), and scavenged groups based on their dissolved (d) concentration–depth profiles (Bruland and Lohan, 2003; Chester, 2000). Scavenged group elements are adsorbed on particles and removed from the ocean with a short residence time of ~10^2–10^3 years, resulting in high concentrations near the sources. In a broad sense, aluminum (Al), manganese (Mn), cobalt

(Co), and lead (Pb) are classified as the scavenged elements.

Aluminum is supplied to the ocean surface via the deposition of atmospheric dust (Hydes, 1979; Maring and Duce, 1987). The surface dAl concentration in the Pacific is as low as a tenth of that in the tropical and subtropical North Atlantic, because the Pacific receives less dust per unit area (Bruland et al., 1994; Measures et al., 2005; Measures and Vink, 2000; Orians and Bruland, 1986). Another important transporter of Al is currents, particularly in the equatorial Pacific (Kaupp et al., 2011; Slemons et al., 2012). Dissolved and particulate Al are transported eastward by the Equatorial Under Current (EUC) from the northeastern coastal margins of New Guinea and New Ireland (Kaupp et al., 2011; Slemons et al., 2012). Supply of Al by tropical and subtropical currents is also observed in the Indian Ocean (Vu and Sohrin, 2013). Other examples would be dAl in Mediterranean Outflow Water (MOW) (Kramer et al., 2004) and in North Atlantic Deep Water (NADW) (Middag et al., 2015). Dissolved Al is removed from the water column by passive adsorption onto particles or active uptake (e.g. diatoms) (Mackenzie et al., 1978; Moran and Moore, 1988). Gehlen et al. (2002) reported direct evidence for the structural association of Al and silicon (Si) in biogenic silica. The vertical profiles of dAl in the ocean often exhibit a mid-depth minimum and increasing concentrations towards the sediment-water interface, which is caused by the advection of Al-rich deep water or by the diffusion of Al from sediment pore water (Bruland et al., 1994; Orians and Bruland, 1985, 1986; Zheng et al., 2017). Suspended particulate Al (pAl) in seawater decreases with distance from the North American continent and increases closer to the bottom due to the resuspension of sediments (Orians and Bruland, 1986). As a result of scavenging, the deep-water dAl concentration in the North Pacific is ~40-fold lower than that in the North Atlantic (Orians and Bruland, 1986). Recent GEOTRACES studies have revealed wide variations in the concentration of dAl and pAl in both the intra- and inter-basin scales in the Atlantic Ocean (Barrett et al., 2015; Measures et al., 2015; Middag et al., 2015), the Southern Ocean (Middag et al., 2011b), and the Mediterranean Sea (Rolison et al., 2015).

The dMn commonly has a maximum concentration at the surface and in the oxygen minimum layer, where O_2 falls below 100 μmol kg^{-1} (Boyle et al., 2005; Bruland et al., 1994; Fujishima et al., 2001; Klinkhammer and Bender, 1980; Landing and Bruland, 1980; Martin

and Knauer, 1980; Zheng et al., 2017). Manganese maxima also occur in hydrothermal plumes in deep water (Boyle et al., 2005; Coale et al., 1991; Klinkhammer, 1980) and in bottom water at the continental margins (Biller and Bruland, 2013; Chase et al., 2005; Minakawa et al., 1998; Slemons et al., 2012). These dMn maxima are related to reductions of Mn(IV) or Mn(III) to soluble Mn(II). Manganese(IV) is reduced via photoreduction in surface water (Sunda and Huntsman, 1988), by microorganisms in sediments (Froelich et al., 1979), and by seawater–basalt interaction during hydrothermal circulation (Von Damm and Bischoff, 1987). Horizontal sections off of North America indicate that Mn is actively remobilized from anoxic sediments on the continental shelves and slopes, diffused into the overlying seawater, and transported by lateral advection (Jones and Murray, 1985; Martin and Knauer, 1984; Martin et al., 1985). Oxidation of Mn(II) is microbially catalyzed, resulting in fast scavenging from a water column (Cowen et al., 1990; Mandernack et al., 1995; Moffett and Ho, 1996). Recent GEOTRACES investigations revealed sectional distributions of Mn in the Atlantic Ocean (Noble et al., 2012; van Hulten et al., 2017), in the Southern Ocean (Middag et al., 2011a), and in the Indian Ocean (Vu and Sohrin, 2013).

The profile of dCo was first observed off central California, showing a surface maximum and a strong correlation with dMn (Knauer et al., 1982). Subsequent observations revealed a subsurface dCo maximum at 50–700 m depths (Ezoe et al., 2004; Fujishima et al., 2001; Noble et al., 2008; Zheng et al., 2017). Cobalt is microbially co-oxidized with Mn (Moffett and Ho, 1996), concentrated in manganese oxides, and released into water through manganese reduction (Biller and Bruland, 2013). Recent studies have indicated the correlation between dCo and phosphate in the upper water column, concluding that dCo is affected by both nutrient cycling and scavenging onto manganese oxides (Hawco et al., 2018; Noble et al., 2008; Saito et al., 2017). The latter process concentrates Co in pelagic sediments, manganese nodules, and manganese crusts, resulting in a small d inventory in deep waters.

Nozaki et al. (1976) reported that radioactive ^{210}Pb ($t_{1/2}$ = 22.3 y) in the Pacific surface water has a maximum concentration at ~35°N and 170°E. They explained ^{210}Pb distribution by dust deposition from the atmosphere and scavenging in the water column, estimating the residence time of Pb in surface water to be 1.7 years in the North Pacific

subtropical gyre. Then, Nozaki et al. (1997) evaluated the residence time of ^{210}Pb in the Pacific Deep Water (PDW) to be > 200 years in the central gyre and 50–100 years at the margins. For stable Pb, Schaule and Patterson (1981) studied the concentration of total dissolvable Pb (tdPb) in seawater between Hawaii and California, revealing the first reliable vertical profile of stable Pb in 1976. Lead is supplied to the North Pacific mainly via the atmosphere at a rate of ~50 ng cm^{-2} y^{-1}, which exceeds the prehistoric output flux of authigenic Pb recorded in pelagic sediments by ~170 times (Flegal and Patterson, 1983). Both the ^{206}Pb/^{207}Pb and ^{206}Pb/^{208}Pb ratios in seawater fitted between the isotopic ratios of Australian and North American leads (Flegal et al., 1984). Boyle et al. (2005) reported a tdPb profile at the Hawaii Ocean Time-series (HOT)-A Long-Term Oligotrophic Habitat Assessment (ALOHA) station (22.75°N, 158°W) in 1999 and found an insignificant change in the subsurface maximum concentration from that in 1976. They attributed the remaining Pb in the Pacific water to Asian emissions by high-temperature processes such as coal burning, although leaded gasoline had been abolished in the United States, Canada, and Japan. They also observed a time-series in the mixed layer near the Hawaii Air-Sea Logging Experiment (HALE)-ALOHA mooring site and reported the presence of an annual cycle in the Pb concentration in which it is ~20% higher in the winter months owing to the downward mixing of the winter mixed layer. Wu et al. (2010) reported that the ^{206}Pb/^{207}Pb ratio in the North Pacific abyssal water is substantially lower than the pre-industrial value, suggesting that anthropogenic Pb has invaded and become the predominant Pb source there. Recently, comprehensive data on Pb isotopes in seawater have been reported from the western North Pacific (Gallon et al., 2011; Zurbrick et al., 2017). It was concluded that only three countries—China, Russia, and Japan—have aerosol Pb isotope composition similar to that of seawater and these occupy about 74% of the industrial input to the western North Pacific. The latest data on the distribution of Pb in seawater were obtained from the Philippine Sea (Chien et al., 2017), near the Juan de Fuca Ridge (Zheng et al., 2017), and from the eastern equatorial Pacific (Pinedo-González et al., 2018). Sectional distributions of Pb have been reported in the Atlantic Ocean (Bridgestock et al., 2018; Bridgestock et al., 2016; Noble et al., 2015; Rigaud et al., 2015; Rusiecka et al., 2018; Zurbrick et al., 2018) and the Indian Ocean (Echegoyen et

al., 2014; Lee et al., 2015; Vu and Sohrin, 2013).

These results suggest that Al, Mn, Co, and Pb are strongly controlled by scavenging. However, each element has specific effects such as supply from reductive sources for Mn and Co, nutrient cycling for Co, and anthropogenic contamination for Pb. Simultaneous observation of these elements will serve to understand these specific effects. Studies conducting such observations are, however, limited, owing to challenges to analysis (Zheng et al., 2017). Here, we report the basin-scale and full-depth sectional distributions of Al, Mn, Co, and Pb in the North Pacific for the first time. We observed the distributions of both td and d species of these elements using a multielement analytical method (Minami et al., 2015) without ultraviolet (UV) irradiation during three GEOTRACES Japan cruises. The difference between td and d concentrations is defined as the labile particulate (lp) concentration. The lp species are liberated from particulate phases during sample storage at pH ~2 with added HCl and at room temperature for more than one year. On the basis of the comprehensive dataset, we systematically discuss the biogeochemical cycling of the scavenged elements in the North Pacific.

2. METHODS

2.1. Hydrographic background of the study site

This study was conducted on the following cruises of R/V *Hakuho Maru*: KH-05-2 from August to September 2005, KH-11-7 in July 2011, and KH-12-4 from August to September 2012 (Fig. 1). The map and a number of figures in this paper were prepared using the Ocean Data View software (Schlitzer, 2018). The KH-05-2 cruise was a reconnaissance study by GEOTRACES Japan. KH-11-7 and KH-12-4 were formal studies by GEOTRACES Japan, occupying GEOTRACES sections GP18 (165°E) and GP02 (47°N), respectively. Figure 2 shows the full-depth sectional distributions of salinity, O_2, silicate, phosphate, and tdM along 160°W longitude. The data from 165°E and 47°N are shown in Supplementary Figs. 1 and 2, respectively. Supplementary Figs. 3 and 4 show the sectional distributions of salinity, potential temperature, O_2, silicate, and phosphate at depths of 0–1000 m along

160°W and 165°E, respectively.

In the tropical Pacific, three major zonal surface currents exist (Fig. 1): the westward-flowing South Equatorial Current (SEC) between about 20°S and 3°N (ST01–03), the narrow eastward-flowing North Equatorial Counter Current (NECC) centered at about 5°N (ST04, 05), and the westward-flowing North Equatorial Current (NEC) between about 8°N and 20°N (ST06, 07) (Wyrtki and Kilonsky, 1984). The EUC is fed by the saline New Guinea Coastal Under Current and flows eastward just below the SEC within a pycnocline at about 200 m depth at ST03 (Supplementary Fig. 3a).

The westward-flowing NEC forms the southern side of the anticyclonic North Pacific subtropical gyre (Fig. 1), splitting into northward and southward boundary currents known as the Kuroshio and Mindanao Currents, respectively. The Kuroshio turns to follow the south coast of Japan and flows eastward at about 35°N to become the Kuroshio Extension (KE), which forms the northern side of the subtropical gyre (Fig. 1). The KE region is between about 30°N and 40°N (TR07–09), where surface water is characterized by high salinity > 34.3 and high temperature > 15°C. Water masses beneath the surface water include the Subtropical Mode Water (STMW) and the Central Mode Water (CMW) with potential density anomaly (σ_θ) values of 25.2–25.8 and 26.0–26.4, respectively (Yasuda, 2003) (Supplementary Fig. 4a). The formation region of the STMW is located at 32–35°N, 140–180°E, and the formation region of CMW is located at 36–43°N, 150°E–160°W. The region between the Kuroshio and the Oyashio is referred to as the Transition Region (TR11, ST11, 12; Fig. 1). The broad eastward flow of this region, known as the North Pacific Current (NPC), includes both the northern side of the subtropical gyre and the southern side of the cyclonic subarctic gyre. At the eastern boundary, the NPC feeds into the southward-flowing California Current (BD17–18) and the northward-flowing Alaska Current.

The western boundary current for the North Pacific subpolar gyre is the Oyashio/East Kamchatka Current (EKC; Fig. 1). The Oyashio separates from the western boundary at about 42°N and flows northeastward as the Oyashio Extension (OE), where surface water is characterized by salinity of 32.7–33.8 and temperature of 0.9–11.1°C (TR13). The subsurface water is the Okhotsk Sea Mode Water (OSMW), at 26.6–27.0 σ_θ, which

originates in the Sea of Okhotsk and flows out to the Pacific through the Kuril Straits (Yasuda, 1997). The OSMW is observed at a depth of about 200 m at TR16/BD07 (Supplementary Fig. 4a). A number of northern stations in this study (TR15, 16, BD07–16, ST13) are located within the subpolar gyre (Fig. 1). The northern side of the gyre is the westward-flowing Alaskan Stream (AS; ST14).

The North Pacific Intermediate Water (NPIW) and the Antarctic Intermediate Water (AAIW) are well-known intermediate water masses in the Pacific Ocean (Talley et al., 2011). Recently, a third main water type at intermediate depths was proposed: the Equatorial Pacific Intermediate Water (EqPIW) (Bostock et al., 2010). The NPIW, which is characterized by a salinity minimum of 33.8, low O_2 at 50–150 μmol kg^{-1}, and low density of 26.4–27.2 σ_θ, averaging 26.8 σ_θ, originates from the OSMW (Yasuda, 1997). The NPIW spreads over the subtropical gyre at a depth range of 400–800 m, bounded by the subarctic front to the north at ~40°N (ST11) and a steep potential vorticity gradient to the south at 15–20°N (ST07; Fig. 2a and Supplementary Fig. 3a). The AAIW is a distinct water mass with high O_2 concentrations of 200–250 μmol kg^{-1}, salinity minima of 34.3–34.5, and a temperature range of 3.5–10°C, resulting in an average density of 27.1 σ_θ. The AAIW forms below the subantarctic front and is then subducted along an isopycnal surface at depths of 600–1300 m. The EqPIW is characterized by low O_2 on the 26.8–27.2 σ_θ isopycnals (ST01–06; Fig. 2a and Supplementary Fig. 3a). The geochemistry of the EqPIW suggests that it is composed primarily of a combination of AAIW and upwelled PDW (Bostock et al., 2010).

In the deep ocean, the Lower and Upper Circumpolar Deep Waters (LCDW and UCDW, respectively) are transported to the North Pacific from the Antarctic Circumpolar Current (Fig. 2c). The LCDW is characterized by a temperature range of 1–2°C, salinity of 34.7, density of 27.8 σ_θ, and the salinity maximum (Talley et al., 2011). The UCDW is characterized by a temperature of 2.5°C, salinity of 34.6, density of 27.6 σ_θ, and the O_2 minimum. The LCDW enters the Central Pacific Basin through the Samoan Passage, proceeds farther north, and reaches the Northeast Pacific Basin (Kawabe and Fujio, 2010) (Fig. 4a). The major branch flows anticyclonically along the Japan, Kuril–Kamchatka, and Aleutian Trenches. The LCDW finally upwells and is transformed into the PDW, which is

233 internally formed entirely in the Pacific from the upwelling and diffusion of the LCDW. The
234 PDW has physical properties similar to those of the UCDW but is enriched with nutrients. It
235 shifts southward in the upper deep layer and is modified by mixing with the UCDW around
236 the Hawaiian Islands (Fig. 2c).
237
238 2.2. Sampling and analysis
239 Seawater samples were collected during the three GEOTRACES Japan cruises
240 (KH-05-2, KH-11-7, and KH-12-4) using a clean sampling system (Sohrin and Bruland,
241 2011). The system was based on a Carousel Water Sampler Frame (SBE-32, Sea-Bird
242 Scientific, USA) that was finished with epoxy paint and equipped with conductivity,
243 temperature, and depth (CTD) sensors (SBE-9-plus, Sea-Bird) and Niskin-X bottles (General
244 Oceanics, USA). The insides of the Niskin bottles were coated with Teflon and were cleaned
245 with 1% detergent, 0.1 mol kg^{-1} hydrochloric acid, and deionized water prepared with a
246 Milli-Q system (MQW; Merck Millipore, Germany) at the beginning of the cruises. The clean
247 sampling system was deployed using a titanium-armored cable. Seawater temperature was
248 measured with the CTD sensor. Salinity reported in this paper was determined using a bench
249 salinometer that was standardized on the basis of the IAPSO standard seawater; the O_2
250 content was measured using the Winkler method; and nutrient concentrations were
251 determined by spectrophotometry using an automated analyzer onboard the vessel. These
252 measurements were in accordance with the protocols for JGOFS (Knap et al., 1996). Nutrient
253 data were checked using seawater reference nutrient material (KANSO, Japan).
254 During KH-05-2, seawater was transferred from the sampler to precleaned Nalgene
255 low-density polyethylene (LDPE) bottles (Thermo Fisher Scientific, USA) on deck using a
256 silicon tube and filling bell to avoid contamination by airborne particles. The samples were
257 immediately transferred into a cleanroom laboratory (class 100) on the vessel. A portion of
258 the seawater for dissolved metal (dM) species was passed through a polycarbonate Nuclepore
259 filter with a pore size of 0.2 µm and a diameter of 47 mm (Whatman, UK) using a closed
260 filtration system. The filter was precleaned with mixtures of HCl–H_2O_2 and HCl–HNO_3–HF
261 (Nakatsuka et al., 2007). The filtered seawater was acidified to pH 2.2 with ultrapure HCl

(Tamapure AA-10, Tama Chemicals, Japan). The portion of the seawater for total dissolvable metal (tdM) species analysis was acidified without filtration. These samples were stored at ambient temperature for ~10 years before analysis.

During KH-11-7 and KH-12-4, the Niskin bottles were carried into a clean bubble upon retrieval of the CTD sampling system, and the seawater samples were transferred from the Niskin bottles to precleaned LDPE bottles. During KH-11-7, filtration was conducted using a Nuclepore filter in a manner similar to that used during KH-05-2. During KH-12-4, filtration was conducted using an AcroPak capsule filter with a pore size of 0.2 µm (Pall, USA), which was directly attached to the Niskin bottle. The seawater samples for both d and td species analyses were immediately acidified in a manner similar to that used during KH-05-2 and were stored at ambient temperature for at least one year before analysis.

An off-line automated solid-phase extraction system (SPE-100, Hiranuma Sangyo, Japan) equipped with a column of Nobias Chelate-PA1 resin (Hitachi High Technologies, Japan) was used for the preconcentration of Al, Mn, iron (Fe), Co, nickel (Ni), copper (Cu), zinc (Zn), cadmium (Cd), and Pb from the seawater (Minami et al., 2015). The seawater samples were adjusted to pH 6.00 ± 0.05 just before preconcentration by adding HAcO–NH_4AcO buffer solution prepared from ultrapure HAcO and NH_3 (TAMAPURE AA-10 or Optima Acids, Thermo Fisher Scientific). When preconcentrating the tdM species, unfiltered samples were first passed through a Millex syringe filter with a pore size of 0.45 µm (Merck Millipore, Germany) and then introduced into the SPE-100. The nine metals were eluted with 1.0 mol kg^{-1} HNO_3 (Optima Acids) and determined with a high-resolution inductively coupled plasma mass spectrometer (HR-ICP-MS, Element 2, Thermo Fisher Scientific) using a calibration curve.

It has been reported that UV irradiation prior to preconcentration is necessary for analysis of total dCo (Biller and Bruland, 2012; Milne et al., 2010; Saito and Moffett, 2001). The UV irradiation is adopted in the Sampling and Sample-handling Protocols for the GEOTRACES Cruises. However, we refrained from using UV irradiation to minimize contamination of the nine metals and to avoid unknown effects of UV irradiation on the determination of the nine metals. So far, we have done two runs of experiment to investigate

291 the effect of UV irradiation on the determination of the nine metals. A portion of the surface
292 seawater sample collected from the North Pacific was taken in a PFA jar with a quartz
293 window and exposed to a 20 mW cm^{-2} lamp for 2–24 h. We found that the concentration of
294 Al and Fe sometimes decreased due to unknown effects of UV irradiation. Recently, Wuttig et
295 al. (2019) studied the effect of UV irradiation and suggested that it should not be performed
296 on samples in which multiple elements are to be determined in order to avoid unnecessary
297 container leaching or contamination. Thus, it should be noted that our Co data are operational
298 results.

299 We evaluated the procedure blanks by using MQW as a sample. The MQW was
300 initially acidified with HCl and then adjusted to pH 6.00 for preconcentration, which is a
301 process similar to that used for seawater samples. We detected contamination during the
302 filtration using a Nuclepore filter for KH-05-2 and KH-11-7. To eliminate this effect, a
303 filtration method similar to that used for seawater was applied to MQW for evaluation of the
304 procedure blanks for dM. We defined the detection limits for tdM and dM as three times the
305 standard deviation (sd) of the procedure blank. The lpM concentrations were obtained by
306 taking the difference between tdM and dM. Because the relative standard deviation (rsd) was
307 ~5% for both tdM and dM, the detection limit of lpM was defined by using the following
308 equation considering the propagation of uncertainty: $2 \times \sqrt{2} \times 0.05 \times C_{ave}$, where C_{ave}
309 represents the average concentration of each dM in this study. The procedure blanks and
310 detection limits are summarized in Supplementary Table 1. We measured the certified
311 reference materials for the trace metals, CASS-5 and NASS-6 (National Research Council
312 Canada), and GEOTRACES open-ocean reference samples SAFe-D2, GS, and GD at an early
313 point in the study (Minami et al., 2015). We participated in the intercalibration campaign of
314 new reference materials of CASS-6 and NASS-7, contributing to the establishment of
315 certified values at a late point in the study (Yang et al., 2018). Recently, we measured new
316 GEOTRACES reference samples, GSP and GSC1. All of these data ensured the accuracy of
317 the trace metal data collected in this study (Supplementary Table 2). A part of our data (dMn
318 and dPb from GP02 and GP18) has been accepted for the GEOTRACES Intermediate Data
319 Product 2017 (Schlitzer et al., 2018). The data on Fe, Ni, Cu, Zn, and Cd will be reported in

forthcoming papers.

3. RESULTS

The seawater data are summarized in Supplementary Table 3. At stations ST01 and 02 of KH-05-2 and TR 07, 11, 13, and 15 of KH-11-7, the vertical profiles of dAl showed abnormal maxima higher than 1 nmol kg^{-1} at intermediate depths, suggesting that contamination from the filtration system occurred at the beginning of each cruise. The dPb data at TR07 were also questionable due to the contamination. Some samples showed abnormally high values of both tdM and dM concentrations, particularly for Pb, suggesting that contamination occurred during sampling. These questionable data have been removed from the discussion. The summary of the seawater data is presented in Table 1. Figure 2 and Supplementary Figs. 1 and 2 show the full-depth sectional distributions of salinity, O_2, silicate, phosphate, and tdM along 160°W, 165°E (GEOTRACES section GP18), and 47°N (GP02), respectively. Figure 3 and Supplementary Figs. 5 and 6 show sectional distributions of dM and lpM for depths of 0–1000 m. The local distributions around the Juan de Fuca Ridge have been reported in a previous paper (Zheng et al., 2017).

3.1. Aluminum

The tdAl concentration was as low as about 1 nmol kg^{-1} at 40–50°N, at 0–4000 m depth in the 160°W section (Fig. 2e). It steeply increased up to 60 nmol kg^{-1} above 50°N due to supply from the continental shelf and slop. In the southern deep waters at > 4000 m depths, an elevated tdAl concentration was observed with a high O_2 concentration, suggesting that it was supplied by the LCDW flowing northward from the Southern Ocean. High tdAl concentrations in deep waters were also found to the north of 40°N, where the LCDW flows eastward (Fig. 4). In the upper section, dAl maxima near 8 nmol kg^{-1} were located at a depth of 200 m at the equator, and at the surface at 15–20°N (Fig. 3a). They correspond to the EUC and NEC, respectively. In contrast, the supply from the northern boundary was dominated by lpAl (Fig. 3e).

In the sections along 165°E and 47°N, tdAl was also high below the depth of 4400 m (Supplementary Figs. 1e and 2e). The tdAl species was dominated by lpAl near the Kamchatka Peninsula (Figs. 7a and b), the Aleutian Islands (Fig. 6a and Supplementary Fig. 7a), and the Juan de Fuca Ridge (Zheng et al., 2017).

Figures 4a and 4b show the horizontal distribution of tdAl and dAl, respectively, at a depth of 4500 m where the LCDW flows. Our data are not enough to cover the whole area of the North Pacific. However, it is apparent that the tdAl concentration tends to be high along the main path of LPDW. Some local sources are found near the Hawaiian Islands, off of the Kamchatka Peninsula, and off of the Aleutian Islands. In contrast, the dAl distribution shows a zonal characteristic. The dAl concentration decreases with latitude, suggesting that there are no strong local sources at high latitudes.

3.2. Manganese

The tdMn concentration was uniformly low at 0.2–0.3 nmol kg^{-1} in deep waters along 160°W, with an increase of up to 1 nmol kg^{-1} in the LCDW (Fig. 2f). High tdMn values of up to 12 nmol kg^{-1} occurred near the continental shelf of the Aleutian Islands. In the upper section, surface maxima of dMn were found in surface water where the SEC and NEC flow (Fig. 3b). Dissolved Mn was as high as 8 nmol kg^{-1} in surface water at the northernmost station ST14 in the AS, and spreaded downwards along an isopycnic surface of about 27.0 σ_θ. In contrast, a significant lpMn maximum was observed only in surface water at ST14 (Fig. 3f).

Elevated tdMn and dMn concentrations also occurred in surface waters to the north of 45°N along 165°E (Supplementary Figs. 1f and 5a) and at the western and eastern ends along 47°N (Supplementary Figs. 2f and 6b), suggesting sources on the continental shelves. In addition, high tdMn and dMn concentrations occurred in bottom water at TR16 near the Kamchatka Peninsula (Supplementary Figs. 1f and 2f) and at middle depths of 1780–3700 m around the Juan de Fuca Ridge (Zheng et al., 2017). In deep waters, tdMn was dominated by lpMn and showed a similar distribution with tdAl (Supplementary Figs. 1f and 2f).

3.3. Cobalt

The concentrations of tdCo and dCo were remarkably high, up to 220 pmol kg^{-1} in the AS, similar to tdMn and dMn (Figs. 2g and 3c). Cobalt spreaded much more widely than Mn in a zone of 26.5–27.0 σ_θ, where the NPIW and the EqPIW existed. In the upper section, dCo was depleted in surface water from 10°S to 40°N in contrast with dMn, suggesting uptake by phytoplankton (Fig. 3c). The lpCo concentration showed some surface maxima along 160°W and abrupt increase at the northern boundary (Fig. 3g).

The concentrations of tdCo and dCo were as high as 90 pmol kg^{-1} in shallow water along the Kamchatka Peninsula and extended along a zone of 26.5–27.0 σ_θ (Supplementary Figs. 1g and 5b). Along 47°N, tdCo and dCo showed maxima in surface water at the western and eastern ends, similar to tdMn and dMn (Supplementary Figs. 2g and 6c); however, tdCo and dCo were distributed more uniformly at intermediate depths. The lpCo concentration showed bottom maxima similar to those of lpAl in the three sections, while the maximum lpCo concentration was less than 20 pmol kg^{-1}. A high concentration of lpCo was also observed in the bottom water around the Juan de Fuca Ridge, although an increase in dCo was not observed (Zheng et al., 2017).

Figure 5a shows the horizontal distribution of tdCo along the isopycnal surface of 26.8 σ_θ. It appears that tdCo has sources on continental shelves and spreads up to the equatorial Pacific. A similar figure for tdMn indicates the same continental shelf sources for tdMn as tdCo. However, the spreading of tdMn is unclear south of 40°N.

3.4. Lead

The tdPb concentration was uniformly low at < 24 pmol kg^{-1} below the depth of 2000 m along 160°W (Fig. 2h). This is similar to that for tdCo. However, tdPb had a unique subsurface maximum between 15°N and 50°N at 160°W. The tdPb species were dominated by dPb, and the maxima of dPb, as high as 80 pmol kg^{-1}, occurred in surface water, the STMW, and the CMW (Fig. 3d).

The maxima of tdPb and dPb in surface and subsurface water were also apparent south of 42°N at 165°E, which is located above the maxima of tdCo and dCo along the NPIW

(Supplementary Figs. 1h and 5c). The maxima of tdPb and dPb were weaker in the section along 47°N (Supplementary Figs. 2h and 6d). Labile particulate Pb was usually undetectable, while it was detected in patches in surface water and in a hydrothermal plume near the Juan de Fuca Ridge (Zheng et al., 2017).

Figure 5b shows the horizontal distribution of the maximum tdPb concentration through the water column. The maximum tdPb concentration usually occurs at subsurface. The tdPb maximum decreases and the corresponding σ_θ increases from west to east: for example, the tdPb maximum is 89.7 pmol kg^{-1} at 25.31 σ_0, TR7 (165°E), 81.6 pmol kg^{-1} at 25.97 σ_0, ST10 (160°W), and 76.9 pmol kg^{-1} at 26.26 σ_0, BD17 (132.7°W).

Table 2 summarizes the metal concentrations in each water mass in the North Pacific Ocean. It is apparent that each metal concentration is uniquely related with the water masses.

4. DISCUSSION

4.1. Comparison at crossover stations and with previously published data

In the GEOTRACES program, a crossover station is a location where the track of one cruise overlaps with that of another cruise, although the research vessels do not have to be at the same location simultaneously (http://www.geotraces.org). Concentrations of dM in the deep ocean are not expected to change significantly on the time scale between cruises; thus, comparing results from crossover stations provides a measure of internal consistency. There are no strict crossover stations between cruises KH-05-2 and KH-12-4. However, stations ST13 and 14 of KH-05-2 are located at about 100 km and 300 km from BD15 of KH-12-4 (160°W, 50.8°N), respectively. Thus, we can use the vertical profiles at these stations for intracomparison. Figure 6 and Supplementary Fig. 7 show the vertical profiles of tdM and dM, respectively, at these stations. For Mn and Co, the vertical profiles of tdM and dM were mostly consistent between stations ST13 and BD15. Both tdM and dM showed good linearity with a slope close to unity (Supplementary Fig. 8). These results indicate that no significant changes occurred in the vertical profiles and that the analytical data of KH-05-2 and KH-12-4

436 are consistent for Mn and Co. At ST14, significantly higher concentrations of Mn and Co
437 were observed. ST14 is located about 80 km off the shelf break and above the Aleutian
438 Trench. The high concentrations of Mn and Co in the surface water are supplied by the AS
439 from reductive sources in continental shelf sediments. In deep water of 500–4000 m, Mn and
440 Co are supplied from the continental slope by resuspension of sediments. The distance effect
441 on concentration was most apparent for tdAl (Fig. 6a). A large amount of Al, mostly in lpAl,
442 is supplied from the continental shelf and slope to ST14. Although most of the Al is removed
443 from the water column between ST14 and BD15 by boundary scavenging, the tdAl
444 concentration is still higher at BD15 than at ST13. In contrast, the distance effect was minor
445 for dAl (Supplementary Fig. 7a). A distinct trend was observed for Pb. In deep water,
446 insignificant differences were noted among the three stations in tdPb and dPb concentrations
447 (Fig. 6d and Supplementary Fig. 7d). The concentrations in the surface water increased from
448 the north station to the south station, suggesting that lithogenic and reductive sources have a
449 negligible effect on Pb. In addition, no distance effect was noted on the Pb concentrations in
450 the subsurface maximum at 100–200 m depths. Rather, the subsurface Pb concentrations are
451 dependent on time, decreasing by about 13 pmol kg^{-1} from 2005 to 2012.
452 For KH-11-7 and KH-12-4, stations TR16 and BD07 are occupied at the same
453 position (160°E, 47°N) as a crossover station. Figure 7 and Supplementary Fig. 9 show the
454 vertical profiles of tdM and dM at these stations. Supplementary Fig. 10 shows the
455 relationship of metal concentrations between TR16 and BD07. For Mn, Co, and Pb, the
456 vertical profiles were consistent between the two stations except that the Mn concentrations in
457 the bottom water were higher in 2012 than in 2011. In contrast, both tdAl and dAl were
458 higher in 2011 than in 2012. The same trend was observed for tdFe, which will be reported in
459 the forthcoming paper. We propose a hypothesis that these temporal changes were caused by
460 the earthquake and tsunami. Stations TR16 and BD07 are located about 280 km southeast of
461 the Kuril–Kamchatka Trench, where the Pacific Plate is subducting under the North American
462 Plate and seismic activity is high. The lower maps in Fig. 7 show the distribution of
463 earthquakes with magnitude > 5 that occurred for five months prior to the sampling dates
464 during 2011 and 2012 (data taken from https://earthquake.usgs.gov/). No significant

difference is noted in the seismic activity around the Kuril–Kamchatka Trench between the two periods. A clear difference is the March 11, 2011, earthquake off the Pacific coast of Tohoku, Japan, magnitude 9.1, that occurred at 38.297°N, 142.373°E and its aftershocks. The resulting tsunami inundated a total area of 561 km^2 in Japan (data from Geospatial Information Authority in Japan: http://www.gsi.go.jp/common/000059939.pdf). The tsunami generated turbidity currents, one of which was observed with bottom sensors (Arai et al., 2013). Thirty-six days after the earthquake, observation on the continental slope below the hypocenter revealed increases in the light transmission anomaly and in the Mn concentrations of up to 15–24 nmol kg^{-1} in the bottom water at depths of 3500–5700 m (Kawagucci et al., 2012). Four months after the earthquake, observations in the Japan Trench revealed nepheloid layers extending ~30–50 m above the sea bed and ^{134}Ce from the Fukushima Daiichi nuclear disaster on the sediment surface (Oguri et al., 2013). Because the distance between the seismic center and TR16 is about 1730 km, the effect might have reached TR16 prior to sampling. The high Mn concentrations in 2012 can be explained by a supply from a temporal reductive source that developed on the bottom sediments where a large amount of organic detritus was transported by the tsunami and the following processes. The detailed explanation of the transportation mechanism is a challenge for future research. Increased marine sediment suspension and fluxes following an earthquake have also been observed at other locations (Thunell et al., 1999).

We also compared our data with the literature and found general consistency for each metal; an example is shown in Supplementary Fig. 11. On the basis of these results, we deduced the following four conclusions. First, the preservation period of the samples had no significant effects on the data. Both unfiltered and filtered seawater samples were acidified to pH 2.2 with HCl and were stored at room temperature from one to ten years prior to analyses. No effect of the storage period was found for either tdM and dM at all crossover stations. In addition, a number of samples were analyzed in duplicate without significant changes, depending on the storage period. Thus, we can conclude that both the unfiltered and filtered seawater samples at pH 2.2 are stable for the determination of the trace metals from one to ten years.

Second, although we did not apply UV irradiation prior to the preconcentration, our data on tdCo and dCo are highly reproducible. It has been proposed that UV irradiation prior to preconcentration is necessary to determine the total dCo (Biller and Bruland, 2012; Milne et al., 2010; Saito and Moffett, 2001). Actually, it appears that our dCo concentrations were significantly lower than those for samples collected near the Hawaii Islands, which were subjected to UV irradiation (Supplementary Fig. 11a) (Noble et al., 2008). We applied UV irradiation to a mixed sample of North Pacific surface water and found an increase in dCo concentration by ~20%. The analytical data for the reference seawater samples also show similar results (Supplementary Table 2). Thus, it should be noted that our Co data are operational and may be lower than those with UV irradiation. Some studies reported that the difference between UV irradiated and non-UV irradiated values varies throughout a water column (Noble et al., 2017; Shelley et al., 2010). However, both the tdCo and dCo are reproducible and show systematic trends as described below. The difference caused by UV irradiation will not qualitatively affect the major points of our discussion, such as those on the basis of the enrichment factor (section 4.4) and the Co/Mn ratio (section 4.5). In addition, the non-labile Co that can be detected after UV irradiation has not been identified yet. It is probable that future comparison between Co data with and without UV will contribute to the characterization of non-labile Co. Therefore, we think our Co data will be informative for the community of chemical oceanography research.

Third, it appears that no significant change occurred in the subsurface Pb maximum from 1977 to the present time in the North Pacific. As an example, the vertical profiles of tdPb in 20°N–35°N, 145°W–160°W from 1976 to 2005 are compared in Supplementary Fig. 11b. Because the tdPb concentration depends on the location, it is not easy to extract the temporal change from these data. However, we can say the subsurface tdPb maximum has been maintained at 63–82 pmol kg^{-1} for 30 years in this area. This is an important characteristic in the North Pacific Ocean. In contrast, a substantial decrease in the subsurface Pb maximum has been observed in the North Atlantic. A decrease of ~150 pmol kg^{-1} during 1979–2011 was found near Bermuda, which is attributed to the phase-out of leaded gasoline in the United States and in Europe (Lee et al., 2011). The decline in the Pb concentration in

523 the Atlantic has also been found along the transect GEOTRACES GA-01 (Zurbrick et al.,
524 2018). In the North Pacific, it has been reported that the decreasing supply from gasoline has
525 been canceled out by the growing supply from coal combustion, metal smelting, and
526 municipal solid waste incineration mainly from China, Russia, and Japan (Zurbrick et al.,
527 2017). The same trend has been shown for ice core data (Gross et al., 2012).

528 Finally, our data suggest that crossover stations near the continental shelves, such as
529 TR16 and BD07, are not ideal for intercomparison of scavenged trace metals. These metals
530 are affected by temporal and spatial variations in the ocean boundary environment. Therefore,
531 for unambiguous intercomparison, a crossover station should be located far from the
532 continental shelves and the offshore side of the boundary scavenging zone.

533

534 4.2. Labile particulate and dissolved fractions

535 The lpM concentration is operationally defined as the difference in concentrations
536 between tdM and dM. Data of particulate concentrations are scarce in the North Pacific. In
537 this study, we compared our dM and lpM data from ST09 (30.007°N, 159.996°W) with the
538 dM and particulate M (pM) data from the Vertex IV site (28°N, 155°W) (Bruland et al., 1994).
539 The authors collected particulate samples on a Nuclepore filter with a pore size of 0.3 μm,
540 and analyzed them for the trace metal content of both the 25% acetic acid leachate and the
541 residual refractory fraction that was treated with HCl–HNO_3–HF. Figure 8b shows the results
542 of pAl, which were mostly in the refractory fraction. Our lpAl concentration at ST09 was
543 similar to or higher than the total pAl concentration at Vertex IV. Because ST09 is located
544 about 800 km from the Hawaiian Seamount Chain, it is possible that the total pAl
545 concentration is elevated compared with Vertex IV. This is consistent with the dAl
546 concentration at depths of 2000–3000 m is higher at ST09 than that at Vertex IV (Fig. 8a).
547 Thus, we can expect that lpAl represents a major fraction of total pAl. Supplementary Fig. 12
548 shows the results for dMn and pMn. Although some of the lpMn concentration at ST09 was
549 less than the detection limit, the general trend was similar between lpMn at ST09 and total
550 pMn at Vertex IV, suggesting that lpMn is a good measure of total pMn. The same results
551 were also observed for Fe, which is reported in the forthcoming paper. No data from the

552 literature are available for comparison of pCo and pPb in this area. Around the Juan de Fuca
553 Ridge, we found that the lpFe/lpAl, lpMn/lpAl, lpCo/lpAl, and lpPb/lpAl ratios in the bottom
554 water are close to the ratios of total concentrations in the bottom sediments (Zheng et al.,
555 2017). On the basis of these results, we suggest that lpM represents a major fraction of total
556 pM. We think lpM includes metals desorbed or released from aluminosilicates, metal oxides,
557 and the degradation of phytoplankton and bacteria.

558 Supplementary Fig. 13 shows histograms of the lpM/tdM ratio for each metal in the
559 North Pacific Ocean. It is apparent that the four metals are classified in the scavenged group
560 but have very different speciations among d and p species. The lpAl/tdAl ratio is 0.66 ± 0.31
561 (average ± sd, n = 489), the lpMn/tdMn ratio is 0.24 ± 0.24 (n = 628), the lpCo/tdCo ratio is
562 0.12 ± 0.18 (n = 620), and the lpPb/tdPb ratio is 0.02 ± 0.08 (n = 575). Because Al is the
563 major element in the upper crust, a large amount of lpAl is supplied from the lithosphere to
564 the ocean. Another major factor controlling the lpM/tdM ratio should be adsorption in the
565 ocean. The adsorption is explained by the surface complexation model (Li, 1981). Inorganic
566 minerals such as aluminosilicates and iron hydroxides have surface hydroxide groups that
567 form surface complexes with metal ions. The stability of the surface complex has a linear
568 relationship with the first hydrolysis constant for the metal ion. Because Al forms a trivalent
569 cation in seawater, it has the highest hydrolysis constant, resulting in the highest lpM/tdM
570 ratio. Although the hydrolysis constant of Pb(II) is higher than that of Mn(II) and Co(II) (Li,
571 1981), Mn(II) is most readily oxidized to Mn(III) or Mn(IV) (Mandernack et al., 1995;
572 Moffett and Ho, 1996), resulting in a higher lpM/tdM ratio. Moreover, it is likely that Co(II)
573 is more readily oxidized to Co(III) than Pb(II) is oxidized to Pb(IV), because Co(II) is
574 co-oxidized with Mn(II) via a common microbially catalyzed pathway (Moffett and Ho,
575 1996).

576 The vertical distributions of the lpM/tdM ratio are also distinct among the
577 scavenged elements (Fig. 9). The lpAl/tdAl ratio is uniformly high at high latitudes. The ratio
578 is lower at low latitudes, especially in surface water, probably due to supply of dAl via
579 surface and subsurface currents from lands in the tropical zone where intense weathering
580 occurs. The lpMn/tdMn ratio shows a generally increasing trend with depth, without a

581 significant change with the latitude. This probably reflects the effects of oxidative scavenging
582 throughout the water column. The lpCo/tdCo ratio shows a trend that is generally increasing
583 in deep water, similar to the lpMn/tdMn ratio, while the former is significantly lower than the
584 latter. In addition, high values of the lpCo/tdCo ratio occur in surface water at lower latitudes
585 due to the uptake of dCo by phytoplankton.
586
587 4.3. Lithogenic effects presented by Al
588 Our data show that tdAl is a good tracer of LCDW in the North Pacific (Fig. 2e,
589 Supplementary Figs. 1e and 2e, and Fig. 4a). In Fig. 10, the tdAl concentration is plotted on
590 the temperature–salinity diagram. The graph indicates that waters with $\sigma_\theta > 27.8$ are enriched
591 with tdAl. In particular, tdAl is useful because tracking LCDW in the northern North Pacific
592 is not easy when using conventional oceanographic parameters. Total dissolvable Al is not
593 only supplied by the LCDW from the South Pacific but also added locally by resuspension of
594 sediments in the North Pacific. The relative contributions from transport via LCDW and from
595 resuspension are unclear at present and would be a challenge in future study. In contrast, dAl
596 decreases when the LCDW flows from south to north in the North Pacific (Fig. 4b).
597 Supplementary Fig. 14 shows that the dAl concentration decreases with latitude at depths
598 greater than 4500 m, where the LCDW flows. The LCDW is the only origin of deep water
599 dAl in the North Pacific; no other water supplies dAl to the depths. When the LCDW flows in
600 the North Pacific, dAl is gradually adsorbed onto particles. In addition, lpAl is added to the
601 LCDW by resuspension of bottom sediments during the track, although the supply of dAl
602 from the bottom sediments is negligible. Overall, the dAl concentration in deep waters
603 decreases from about 4 nmol kg^{-1} around the equator to about 1 nmol kg^{-1} around 50°N. It
604 takes about 100 years for the LCDW to travel from the equator to 50°N (Matsumoto, 2007);
605 the apparent decreasing rate of dAl is 0.03 nmol kg^{-1} y^{-1} in deep waters in the North Pacific
606 Ocean.
607
608 4.4. Enrichment factor
609 Here, we use stoichiometry to characterize sources for each element. The

610 enrichment factor (*EF*) of dM in seawater over the upper crust is defined in accordance with
611 the *EF* of M in aerosols in the literature (Rahn, 1976) as follows:

612 $$EF(\mathrm{dM}) = (\mathrm{dM/dAl})_{\mathrm{seawater}}/(\mathrm{M/Al})_{\mathrm{upper\ crust}}$$

613 The $(\mathrm{M/Al})_{\mathrm{upper\ crust}}$ is calculated in moles using concentrations published in a review
614 (Rudnick and Gao, 2005) as the following: 4.7×10^{-3} for Mn, 9.7×10^{-5} for Co, and $2.7 \times$
615 10^{-5} for Pb. Figure 11 shows box plots of *EF*(dM). The median is 1.3×10^{2} (n = 436) for
616 *EF*(dMn), 3.2×10^{2} (n = 430) for *EF*(dCo), and 1.2×10^{3} (n = 413) for *EF*(dPb). The median
617 of *EF*(dPb) is on the same order as that of *EF* for aerosols in the literature (Rahn, 1976),
618 suggesting that aerosols are a major source of dPb. For Mn and Co, the *EF* for aerosols is
619 usually 1–10. Thus, *EF*(dMn) and *EF*(dCo) are ten to hundred times higher than the *EF* for
620 aerosols. This would be partly due to the differences in solubility of the metals in aerosols. As
621 an example, Baker et al. (2006) reported that the solubility of Mn is several to ten times
622 higher than that of Al. Another important cause would be that sources other than aerosols are
623 more significant contributors to Mn and Co. Sectional distributions of *EF*(dM) and *EF*(lpM)
624 along 160°W and 47°N are given in Supplementary Figs. 15 and 16, respectively. These
625 figures show that the other sources of dMn and dCo are restricted to shallow depths near the
626 northern boundaries of the North Pacific.

627 Figure 2 shows the sectional distributions of dM and lpM in the upper ocean along
628 160°W. It is clear that each element has different sources and is uniquely related to the ocean
629 circulation. The dAl concentration is high in the EUC and NEC. The transport of Al by the
630 EUC from New Guinea and New Ireland has been reported in the literature (Kaupp et al.,
631 2011; Slemons et al., 2012). The source of dAl in the NEC should be the Hawaiian Islands.
632 The elevated dAl concertation near the Hawaiian Islands has been reported in the literature
633 (Measures et al., 2005). In contrast, the dAl concentration is low in northern currents, such as
634 the AS. Similarly, high dAl concentrations in tropical currents have been found in the Indian
635 Ocean (Vu and Sohrin, 2013). These results are ascribed to supply of dAl via surface and
636 subsurface currents from lands in the tropical zone where intense weathering occurs. The dMn
637 concentration is high in the AS, suggesting the source is manganese reduction in sediments on
638 the continental shelf. Substantially high dMn concentrations have been observed over the

Bering Sea shelf (Cid et al., 2011). A surface maximum of dMn occurs between 7°N and 26°N, suggesting the effect of photoreduction (Sunda and Huntsman, 1988). The dCo concentration is high in the AS, suggesting the same reductive source with dMn. These results are also consistent with the observation in the Bering Sea (Cid et al., 2011). A remarkable feature of dCo is that it expands through the NPIW and EqPIW over the North Pacific. The subsurface maximum of dPb occurs between 20°N and 45°N, corresponding with the STMW and CMW in the subtropical gyre. Supplementary Figs. 5 and 6 shows the sectional distributions of dM in the upper ocean along 165°E and 47°N, respectively. These distributions also indicate that dMn and dCo are derived from the same sources on the continental shelves, which do not contribute significantly to dPb.

Figure 5 shows distinct horizontal distributions of tdCo and tdPb over the North Pacific. For tdCo, the concentration on an isopycnal plane of 26.8 σ_θ is presented. It is clear that tdCo originated from the northern shelves and spread southward. For tdPb, the highest subsurface concentration maximum is presented because the σ_θ value for the tdPb maximum significantly increases from west to east. The highest tdPb occurs in the subtropical gyre and decreases from west to east. This horizontal distribution of tdPb is consistent with that of radioactive ^{210}Pb in the surface water (Nozaki et al., 1976).

4.5. Redox and biogeochemical control on Co

As discussed above, Co and Mn have a common source in the continental shelf sediments. In hydrothermal plumes around the Juan de Fuca Ridge, the concentration of Mn increases remarkably and that of Co does not. This is because the flux of Mn from hydrothermal vents is considerably higher than that of Co (Seyfried Jr et al., 2003). In addition, the solubility product is much lower for CoS than MnS (Chemical et al., 1964), although the solubility of Co increases with increasing chloride concentration (Seyfried Jr et al., 2003). Thus, Co is not transported far by hydrothermal plumes. Supplementary Fig. 17a shows the relationship between dCo and dMn in water columns above the depth of hydrothermal plumes (σ_θ < 27.64). The following overall linear relationship is present:

$$\text{dCo (pmol kg}^{-1}) = 19.7\ \text{dMn (nmol kg}^{-1}) + 17.2 \quad (r = 0.656,\ p < 0.0001,\ n = 386)$$

This slope is nearly consistent with the ratio of Co/Mn = 2.1×10^{-2} for average mole concentrations in the upper crust (Rudnick and Gao, 2005). These results imply that the ultimate source of Mn and Co in the North Pacific Ocean has a Co/Mn ratio similar to that in the upper crust. However, most data in the graph are along another line with a higher slope, which means that dCo and dMn are substantially fractionated in the North Pacific.

Figure 12 shows that the dCo/dMn ratio varies from zero to 0.174 in the North Pacific. Although both Mn and Co are taken up by phytoplankton as micronutrients, the concentration factor of Co in phytoplankton is much higher than that of Mn (Morel et al., 2003). As a result, the effects of biogeochemical cycles are apparent only in the distribution of Co in the ocean. The dCo concentration is low in the surface water except at stations near continental shelves (Fig. 3c and Supplementary Figs. 5b and 6c). This is ascribed to the uptake of Co by phytoplankton. Supplementary Fig. 17b shows the general relationship of dCo against phosphate in water columns above the depth of the NPIW ($\sigma_\theta < 26.5$):

$$\text{dCo (pmol kg}^{-1}) = 36.4\ \text{PO}_4\ (\mu\text{mol kg}^{-1}) + 6.4 \quad (r = 0.692,\ p < 0.0001,\ n = 176)$$

These results are mostly consistent with the data on total dCo in the literature (Hawco et al., 2018; Noble et al., 2008; Saito et al., 2017), which suggest that dCo is taken up by phytoplankton and is remineralized from settled particles concurrently with phosphate. The dCo/phosphate ratio tends to be higher at higher latitudes. Particularly high ratios were found in the surface water at ST14 in the AS. Biogeochemical effects are also apparent in the vertical distribution of the dCo/dMn ratio (Fig. 12). The ratio becomes lower in surface water according to the selective uptake and removal of dCo by phytoplankton and increases with depth above the NPIW with $\sigma_\theta = 26.8$, through remineralization. Another cause for the high dCo/dMn ratio in waters with $\sigma_\theta > 26$ should be the microbial oxidation of dMn, which is 7–10 times faster than that of dCo (Moffett and Ho, 1996), resulting in the selective transformation from dMn to lpMn. Below the NPIW, no clear relationship is apparent between the dCo and phosphate, and the dCo/dMn ratio decreases. Because the concentrations of O_2 and biogenic particulate organic matter decrease below the NPIW, scavenging becomes predominant over remineralization for the distribution of dCo.

4.6. Anthropogenic control on Pb

In this paper, we report the basin-scale distribution of stable Pb in the North Pacific for the first time. The subsurface maximum centered at ~26 σ_θ is a basin-scale characteristic. The maximum concentration tends to decrease from west to east. In addition, *EF*(dPb) is as high as *EF* for aerosols. These results further support the anthropogenic control on Pb in the North Pacific, which has been discussed in previous research (Boyle et al., 2005; Zurbrick et al., 2017). To summarize, anthropogenic Pb originating from China, Japan, and Russia is carried to the North Pacific as aerosols by westerlies centered at ~35°N, deposited on the sea surface, and dissolved in the mixed layer during formation of the STMW and CMW. Although dPb is quickly scavenged from the surface water by biogenic particles, it has a longer residence time in subsurface water and spreads over the North Pacific by current systems of subtropical and subarctic gyres. This mechanism is not as important for Al, Mn, and Co because these metals are less enriched in industrial aerosols. For example, the enrichment factor of Pb was 10–100 times higher than that of Mn and Co in atmospheric deposition samples collected around Japan (Okubo et al., 2013).

In deep water (σ_θ > 26.7), a linear relationship between dPb and dCo is observed (Fig. 13):

dPb (pmol kg^{-1}) = 1.06 dCo (pmol kg^{-1}) – 3.1 (r = 0.868, p < 0.0001, n = 374)

which suggests the concurrent effect of scavenging. Because there are no significant sources for both metals in deep waters, a common property emerges for the scavenged elements. The dPb/dCo ratio tends to be higher at higher latitudes. This probably reflects the dependency of atmospheric aerosol deposition flux on the latitude. In shallow waters, no significant relationship is observed between dPb and dCo, which reflects different sources for these metals. Clearly, anthropogenic Pb sources contribute to high concentrations mostly in warm surface waters of the temperate zone (Fig. 3d and Supplementary Fig. 5c).

Interestingly, radiocesium emitted from the Fukushima Daiichi Nuclear Power Plant (37°25′N, 141°02′E) in March 2011 presently shows a distribution similar to that of Pb in the North Pacific (Aoyama et al., 2018; Kumamoto et al., 2014; Smith et al., 2017). As an example, Kumamoto et al. (2014) measured d radiocesium at stations along 149°E in winter

2012 (Supplementary Fig. 18). In particular, they found a subsurface radiocesium maximum at a depth of ~300 m around 32°N, which is a characteristic similar to the subsurface maximum of Pb. They concluded that atmosphere-deposited radiocesium south of the KE had been transported not only eastward along with surface currents but also southward owing to the formation/subduction of the STMW within about 10 months after the accident. Smith et al. (2017) reported that the Fukushima-derived radiocesium plume was first observed in June 2012 at the westernmost station on Line P, which is an oceanographic sampling line extending 1500 km westward of British Columbia, Canada. The plume spread over the Canadian continental shelf during 2013 and 2014. It is likely that anthropogenic contaminants in aerosols are entrained in the same distribution mechanism as that for Pb. Although Cs is a conservative element in oceanography, the Fukushima-derived radiocesium followed Pb in the manner of its distribution mechanism and spread over the North Pacific, at least during the first several years after the accident.

5. CONCLUSIONS

We observed basin-scale and full-depth sectional distributions of Al, Mn, Co, and Pb in the North Pacific using a multi-elemental determination method and without using UV irradiation. This study revealed that the speciation of the dM and pM fractions differs significantly among the four metals. Analysis based on stoichiometry revealed that Mn, Co, and Pb are dominated by different sources than those of Al and that each element is a unique tracer for distinct currents and water masses. However, despite the apparent differences, these elements should be grouped as scavenged elements. The four metals are affected by scavenging throughout the ocean, although the relative intensity of the other processes controls the distribution of each metal. As an example, Co and Pb show a strong correlation in the deep waters of the North Pacific, where no significant sources occur for these metals, and scavenging is the predominant process. In contrast, the differences between Co and Mn in terms of the oxidation rate, the enrichment by phytoplankton, and the effect of hydrothermal plumes cause substantial fractionations of dCo and dMn in the North Pacific.

We propose *EF*(dM) as a potential parameter to systematically explain inter-basin variations in the distribution of dM. Dissolved Al occurs in a wider concentration range in the world's oceans than the other metals. Because dAl concentration is normally low in the North Pacific, *EF* is high for dMn, dCo, and dPb, resulting in the unique distribution of each metal. Since dAl concentration is substantially higher in the Atlantic Ocean and the Mediterranean Sea, features common with dAl may emerge for dMn, dCo, and dPb.

ACKNOWLEDGEMENTS

This research was supported by The Japan Society for the Promotion of Science (JSPS) KAKENHI grants (Grant Nos. JP16204046, JP21350042, JP24241004, and JP15H0127), by grants from the Steel Foundation for Environmental Protection Technology, and by Mitsumasa Ito Memorial Research Grant from the Research Institute for Oceanochemistry Foundation. The authors thank the crew, technicians, students, and scientists onboard the KH-05-2, KH-11-7, and KH-12-4 cruises for assistance with sampling and analysis of routine data. We would like to thank Editage (www.editage.jp) for English language editing. Finally, we thank three anonymous reviewers and the associate editor Tina van de Flierdt for their helpful and constructive comments.

776 Figure Captions

777 Fig. 1. A map showing the locations of the data collected in this study. The white lines show
778 surface currents and the dashed line shows the subsurface current.

779

780 Fig. 2. Full-depth sectional distribution of salinity, O_2, silicate, phosphate, and tdM along
781 160°W. EqPIW: Equatorial Pacific Intermediate Water; NPIW: North Pacific Intermediate
782 Water; UCDW: Upper Circumpolar Deep Water; LCDW: Lower Circumpolar Deep Water;
783 PDW: Pacific Deep Water; AS: Alaskan Stream; STMW: Subtropical Mode Water.

784

785 Fig. 3. Sectional distributions of dM and lpM at depths of 0–1000 m along 160°W. EUC:
786 Equatorial Under Current; NEC: North Equatorial Current; AS: Alaskan Stream; EqPIW:
787 Equatorial Pacific Intermediate Water; NPIW: North Pacific Intermediate Water; STMW:
788 Subtropical Mode Water; CMW: Central Mode Water.

789

790 Fig. 4. The distributions of tdAl and dAl at a depth of 4500 m. The red line shows the major
791 flows of the LCDW, which were taken from the literature (Kawabe and Fujio, 2010). A
792 number in a circle shows the volume transport of the current in Sv (10^6 m^3 s^{-1}). The number
793 4^+ (4^-) means a little more (less) than 4 Sv. A circle with a center point shows upwelling from
794 this layer; its transport volume is shown by an accompanying number.

795

796 Fig. 5. (a) The horizontal distribution of tdCo on the isopycnal plane of 26.8 σ_θ. (b) The
797 horizontal distribution of the maximum tdPb in the water column, which occurs in the
798 subsurface water.

799

800 Fig. 6. Vertical profiles of tdM at ST13 (red circles), BD15 (blue squares), and ST14 (cyan
801 diamonds).

802

803 Fig. 7. (a) and (b): The vertical profiles of tdAl and dAl at TR16 (red circles) and BD07 (blue
804 squares). The distribution of earthquakes (magnitude > 5) around the Kuril–Kamchatka

Trench from February 28 to July 28, 2011 (c), and from March 28 to August 28, 2012 (d). A black circle represents a seismic center and the diameter of such a circle represents the relative magnitudes of the earthquakes. The data were taken from https://earthquake.usgs.gov.

Fig. 8. Vertical profiles of dAl and particulate Al (pAl). Red triangles represent dAl and lpAl at ST09 (30.007°N, 159.996°W). Black marks represent data at the Vertex IV site (28°N, 155°W) (Bruland et al., 1994). (b) Open circles, squares, and diamonds represent acetic acid leachable pAl, refractory pAl, and total pAl, respectively.

Fig. 9. Vertical distribution of the lpM/tdM ratio in the North Pacific. The colors of the dots represent the latitudes.

Fig. 10. Potential temperature–salinity diagram. The colors of the dots represent the tdAl concentrations.

Fig. 11. Box plots of *EF*(dM) for Mn, Co, and Pb. The middle line of the box represents the median; the top and bottom lines of the box represent the upper and lower quartiles, respectively; and circles represent potential outliers.

Fig. 12. The tdCo/tdMn ratio against the potential density anomaly in the North Pacific. The colors of the dots represent the latitudes. The black line shows the average Co/Mn mole ratio of 2.1×10^{-2} in the upper crust (Rudnick and Gao, 2005).

Fig. 13. The relationship between dPb and dCo in deep waters ($\sigma_\theta > 26.7$). The red line represents the regression line, the equation for which is presented in the text. The colors of the dots represent the latitudes.

833 REFERENCES

834 Aoyama, M., Hamajima, Y., Inomata, Y., Kumamoto, Y., Oka, E., Tsubono, T. and Tsumune,
835 D. (2018) Radiocaesium derived from the TEPCO Fukushima accident in the North Pacific
836 Ocean: Surface transport processes until 2017. J. Environ. Radioact. 189, 93-102.
837 Arai, K., et al. (2013) Tsunami-generated turbidity current of the 2011 Tohoku-Oki
838 earthquake. Geology 41, 1195-1198.
839 Baker, A.R., Jickells, T.D., Witt, M. and Linge, K.L. (2006) Trends in the solubility of iron,
840 aluminium, manganese and phosphorus in aerosol collected over the Atlantic Ocean. Mar.
841 Chem. 98, 43-58.
842 Barrett, P.M., Resing, J.A., Buck, N.J., Landing, W.M., Morton, P.L. and Shelley, R.U.
843 (2015) Changes in the distribution of Al and particulate Fe along A16N in the eastern North
844 Atlantic Ocean between 2003 and 2013: Implications for changes in dust deposition. Mar.
845 Chem. 177, Part 1, 57-68.
846 Biller, D.V. and Bruland, K.W. (2012) Analysis of Mn, Fe, Co, Ni, Cu, Zn, Cd, and Pb in
847 seawater using the Nobias-chelate PA1 resin and magnetic sector inductively coupled plasma
848 mass spectrometry (ICP-MS). Mar. Chem. 130-131, 12-20.
849 Biller, D.V. and Bruland, K.W. (2013) Sources and distributions of Mn, Fe, Co, Ni, Cu, Zn,
850 and Cd relative to macronutrients along the central California coast during the spring and
851 summer upwelling season. Mar. Chem. 155, 50-70.
852 Bostock, H.C., Opdyke, B.N. and Williams, M.J.M. (2010) Characterising the intermediate
853 depth waters of the Pacific Ocean using d13C and other geochemical tracers. Deep-Sea Res. I
854 57, 847-859.
855 Boyle, E.A., Bergquist, B.A., Kayser, R.A. and Mahowald, N. (2005) Iron, manganese, and
856 lead at Hawaii Ocean Time-series station ALOHA: Temporal variability and an intermediate
857 water hydrothermal plume. Geochim. Cosmochim. Acta 69, 933-952.
858 Bridgestock, L., Rehkämper, M., van de Flierdt, T., Paul, M., Milne, A., Lohan, M.C. and
859 Achterberg, E.P. (2018) The distribution of lead concentrations and isotope compositions in
860 the eastern Tropical Atlantic Ocean. Geochim. Cosmochim. Acta 225, 36-51.
861 Bridgestock, L., et al. (2016) Return of naturally sourced Pb to Atlantic surface waters. Nat.
862 Commun. 7, 12921.
863 Bruland, K.W. and Lohan, M.C. (2003) Controls of Trace Metals in Seawater, in: Elderfield,
864 H. (Ed.), The Oceans and Marine Geochemistry. Elsevier-Pergamon, Oxford, pp. 23-47.
865 Bruland, K.W., Orians, K.J. and Cowen, J.P. (1994) Reactive trace metals in the stratified
866 central North Pacific. Geochim. Cosmochim. Acta 58, 3171-3182.
867 Chase, Z., Johnson, K.S., Elrod, V.A., Plant, J.N., Fitzwater, S.E., Pickell, L. and Sakamoto,
868 C.M. (2005) Manganese and iron distributions off central California influenced by upwelling
869 and shelf width. Mar. Chem. 95, 235-254.
870 Chemical, S., Sillén, L.G. and Martell, A.E. (1964) Stability constants of metal-ion complexes.

Chemical Society.
Chester, R. (2000) Marine Geochemistry, 2nd ed. Blackwell, Malden.
Chien, C.-T., Ho, T.-Y., Sanborn, M.E., Yin, Q.-Z. and Paytan, A. (2017) Lead concentrations and isotopic compositions in the Western Philippine Sea. Mar. Chem. 189, 10-16.
Cid, A.P., Urushihara, S., Minami, T., Norisuye, K. and Sohrin, Y. (2011) Stoichiometry among bioactive trace metals in seawater on the Bering Sea shelf. J. Oceanogr. 67, 747-764.
Coale, K.H., Chin, C.S., Massoth, G.J., Johnson, K.S. and Baker, E.T. (1991) In situ chemical mapping of dissolved iron and manganese in hydrothermal plumes. Nature 352, 325-328.
Cowen, J.P., Massoth, G.J. and Feely, R.A. (1990) Scavenging rates of dissolved manganese in a hydrothermal vent plume. Deep-Sea Res. A 37, 1619-1637.
Echegoyen, Y., Boyle, E.A., Lee, J.-M., Gamo, T., Obata, H. and Norisuye, K. (2014) Recent distribution of lead in the Indian Ocean reflects the impact of regional emissions. Proc. Natl. Acad. Sci. USA 111, 15328-15331.
Ezoe, M., Ishita, T., Kinugasa, M., Lai, X., Norisuye, K. and Sohrin, Y. (2004) Distributions of dissolved and acid-dissolvable bioactive trace metals in the North Pacific Ocean. Geochem. J. 38, 535-550.
Flegal, A.R. and Patterson, C.C. (1983) Vertical concentration profiles of lead in the Central Pacific at 15°N and 20°S. Earth Planet. Sci. Lett. 64, 19-32.
Flegal, A.R., Schaule, B.K. and Patterson, C.C. (1984) Stable isotopic ratios of lead in surface waters of the Central Pacific. Mar. Chem. 14, 281-287.
Froelich, P.N., et al. (1979) Early oxidation of organic matter in pelagic sediments of the eastern equatorial Atlantic: suboxic diagenesis. Geochim. Cosmochim. Acta 43, 1075-1090.
Fujishima, Y., Ueda, K., Maruo, M., Nakayama, E., Tokutome, C., Hasegawa, H., Matsui, M. and Sohrin, Y. (2001) Distribution of Trace Bioelements in the Subarctic North Pacific Ocean and the Bering Sea (the R/V Hakuho Maru Cruise KH-97-2). J. Oceanogr. 57, 261-273.
Gallon, C., Ranville, M.A., Conaway, C.H., Landing, W.M., Buck, C.S., Morton, P.L. and Flegal, A.R. (2011) Asian Industrial Lead Inputs to the North Pacific Evidenced by Lead Concentrations and Isotopic Compositions in Surface Waters and Aerosols. Environ. Sci. Technol. 45, 9874-9882.
Gehlen, M., Beck, L., Calas, G., Flank, A.M., Van Bennekom, A.J. and Van Beusekom, J.E.E. (2002) Unraveling the atomic structure of biogenic silica: evidence of the structural association of Al and Si in diatom frustules. Geochim. Cosmochim. Acta 66, 1601-1609.
Gross, B.H., Kreutz, K.J., Osterberg, E.C., McConnell, J.R., Handley, M., Wake, C.P. and Yalcin, K. (2012) Constraining recent lead pollution sources in the North Pacific using ice core stable lead isotopes. J. Geophys. Res.: Atmospheres 117, D16307.
Hawco, N.J., Lam, P.J., Lee, J.-M., Ohnemus, D.C., Noble, A.E., Wyatt, N.J., Lohan, M.C. and Saito, M.A. (2018) Cobalt scavenging in the mesopelagic ocean and its influence on global mass balance: Synthesizing water column and sedimentary fluxes. Mar. Chem. 201,

151-166.
Hydes, D.J. (1979) Aluminum in Seawater: Control by Inorganic Processes. Science 205, 1260-1262.
Jones, C.J. and Murray, J.W. (1985) The geochemistry of manganese in the northeast Pacific Ocean off Washington. Limnol. Oceanogr. 30, 81-92.
Kaupp, L.J., Measures, C.I., Selph, K.E. and Mackenzie, F.T. (2011) The distribution of dissolved Fe and Al in the upper waters of the Eastern Equatorial Pacific. Deep-Sea Res. II 58, 296-310.
Kawabe, M. and Fujio, S. (2010) Pacific ocean circulation based on observation. J. Oceanogr. 66, 389-403.
Kawagucci, S., et al. (2012) Disturbance of deep-sea environments induced by the M9.0 Tohoku Earthquake. Sci. Rep. 2, 270.
Klinkhammer, G.P. (1980) Observations of the distribution of manganese over the East Pacific Rise. Chem. Geol. 29, 211-226.
Klinkhammer, G.P. and Bender, M.L. (1980) The distribution of manganese in the Pacific Ocean. Earth Planet. Sci. Lett. 46, 361-384.
Knap, A.H., Michaels, A., Close, A.R., Ducklow, H. and Dickson, A.G. (1996) Protocols for the Joint Global Ocean Flux Study (JGOFS) Core Measurements.
Knauer, G.A., Martin, J.H. and Gordon, R.M. (1982) Cobalt in north-east Pacific waters. Nature 297, 49-51.
Kramer, J., Laan, P., Sarthou, G., Timmermans, K.R. and de Baar, H.J.W. (2004) Distribution of dissolved aluminium in the high atmospheric input region of the subtropical waters of the North Atlantic Ocean. Mar. Chem. 88, 85-101.
Kumamoto, Y., Aoyama, M., Hamajima, Y., Aono, T., Kouketsu, S., Murata, A. and Kawano, T. (2014) Southward spreading of the Fukushima-derived radiocesium across the Kuroshio Extension in the North Pacific. Sci. Rep. 4, 4276.
Landing, W.M. and Bruland, K.W. (1980) Manganese in the North Pacific. Earth Planet. Sci. Lett. 49, 45-56.
Lee, J.-M., Boyle, E.A., Echegoyen-Sanz, Y., Fitzsimmons, J.N., Zhang, R. and Kayser, R.A. (2011) Analysis of trace metals (Cu, Cd, Pb, and Fe) in seawater using single batch nitrilotriacetate resin extraction and isotope dilution inductively coupled plasma mass spectrometry. Anal. Chim. Acta 686, 93-101.
Lee, J.-M., Boyle, E.A., Gamo, T., Obata, H., Norisuye, K. and Echegoyen, Y. (2015) Impact of anthropogenic Pb and ocean circulation on the recent distribution of Pb isotopes in the Indian Ocean. Geochim. Cosmochim. Acta 170, 126-144.
Li, Y.-H. (1981) Ultimate removal mechanisms of elements from the ocean. Geochim. Cosmochim. Acta 45, 1659-1664.
Mackenzie, F.T., Stoffyn, M. and Wollast, R. (1978) Aluminum in Seawater: Control by Biological Activity. Science 199, 680.

949 Mandernack, K.W., Post, J. and Tebo, B.M. (1995) Manganese mineral formation by bacterial
950 spores of the marine Bacillus, strain SG-1: Evidence for the direct oxidation of Mn(II) to
951 Mn(IV). Geochim. Cosmochim. Acta 59, 4393-4408.
952 Maring, H.B. and Duce, R.A. (1987) The impact of atmospheric aerosols on trace metal
953 chemistry in open ocean surface seawater, 1. Aluminum. Earth Planet. Sci. Lett. 84, 381-392.
954 Martin, J.H. and Knauer, G.A. (1980) Manganese cycling in northeast Pacific waters. Earth
955 Planet. Sci. Lett. 51, 266-274.
956 Martin, J.H. and Knauer, G.A. (1984) VERTEX: manganese transport through oxygen
957 minima. Earth Planet. Sci. Lett. 67, 35-47.
958 Martin, J.H., Knauer, G.A. and Broenkow, W.W. (1985) VERTEX: the lateral transport of
959 manganese in the northeast Pacific. Deep-Sea Res. A 32, 1405-1427.
960 Matsumoto, K. (2007) Radiocarbon-based circulation age of the world oceans. J. Geophys.
961 Res. 112, C09004.
962 Measures, C., Hatta, M., Fitzsimmons, J. and Morton, P. (2015) Dissolved Al in the zonal N
963 Atlantic section of the US GEOTRACES 2010/2011 cruises and the importance of
964 hydrothermal inputs. Deep-Sea Res. II 116, 176-186.
965 Measures, C.I., Brown, M.T. and Vink, S. (2005) Dust deposition to the surface waters of the
966 western and central North Pacific inferred from surface water dissolved aluminum
967 concentrations. Geochem. Geophys. Geosyst. 6, Q09M03.
968 Measures, C.I. and Vink, S. (2000) On the use of dissolved aluminum in surface waters to
969 estimate dust deposition to the ocean. Global Biogeochem. Cycles 14, 317-327.
970 Middag, R., de Baar, H.J.W., Laan, P., Cai, P.H. and van Ooijen, J.C. (2011a) Dissolved
971 manganese in the Atlantic sector of the Southern Ocean. Deep-Sea Res. II 58, 2661-2677.
972 Middag, R., van Hulten, M.M.P., Van Aken, H.M., Rijkenberg, M.J.A., Gerringa, L.J.A.,
973 Laan, P. and de Baar, H.J.W. (2015) Dissolved aluminium in the ocean conveyor of the West
974 Atlantic Ocean: Effects of the biological cycle, scavenging, sediment resuspension and
975 hydrography. Mar. Chem. 177, Part 1, 69-86.
976 Middag, R., van Slooten, C., de Baar, H.J.W. and Laan, P. (2011b) Dissolved aluminium in
977 the Southern Ocean. Deep-Sea Res. II 58, 2647-2660.
978 Milne, A., Landing, W., Bizimis, M. and Morton, P. (2010) Determination of Mn, Fe, Co, Ni,
979 Cu, Zn, Cd and Pb in seawater using high resolution magnetic sector inductively coupled
980 mass spectrometry (HR-ICP-MS). Anal. Chim. Acta 665, 200-207.
981 Minakawa, M., Noriki, S. and Tsunogai, S. (1998) Manganese in the Bering Sea and the
982 northern North Pacific Ocean. Geochem. J. 32, 315-329.
983 Minami, T., Konagaya, W., Zheng, L., Takano, S., Sasaki, M., Murata, R., Nakaguchi, Y. and
984 Sohrin, Y. (2015) An off-line automated preconcentration system with
985 ethylenediaminetriacetate chelating resin for the determination of trace metals in seawater by
986 high-resolution inductively coupled plasma mass spectrometry. Anal. Chim. Acta 854,
987 183-190.

988 Moffett, J.W. and Ho, J. (1996) Oxidation of cobalt and manganese in seawater via a common
989 microbially catalyzed pathway. Geochim. Cosmochim. Acta 60, 3415-3424.
990 Moran, S.B. and Moore, R.M. (1988) Evidence from mesocosm studies for biological
991 removal of dissolved aluminium from sea water. Nature 335, 706-708.
992 Morel, F.M.M., Milligan, A.J. and Saito, M.A. (2003) Marine bioinorganic chemistry: the
993 role of trace metals in the oceanic cycles of major nutrients, in: Elderfield, H. (Ed.), The
994 Oceans and Marine Geochemistry. Elsevier-Pergamon, Oxford, pp. 113-143.
995 Nakatsuka, S., Okamura, K., Norisuye, K. and Sohrin, Y. (2007) Simultaneous determination
996 of suspended particulate trace metals (Co, Ni, Cu, Zn, Cd and Pb) in seawater with small
997 volume filtration assisted by microwave digestion and flow injection inductively coupled
998 plasma mass spectrometer. Anal. Chim. Acta 594, 52-60.
999 Noble, A.E., Echegoyen-Sanz, Y., Boyle, E.A., Ohnemus, D.C., Lam, P.J., Kayser, R., Reuer,
1000 M., Wu, J. and Smethie, W. (2015) Dynamic variability of dissolved Pb and Pb isotope
1001 composition from the U.S. North Atlantic GEOTRACES transect. Deep-Sea Res. II 116,
1002 208-225.
1003 Noble, A.E., et al. (2012) Basin-scale inputs of cobalt, iron, and manganese from the
1004 Benguela-Angola front to the South Atlantic Ocean. Limnol. Oceanogr. 57, 989-1010.
1005 Noble, A.E., Ohnemus, D.C., Hawco, N.J., Lam, P.J. and Saito, M.A. (2017) Coastal sources,
1006 sinks and strong organic complexation of dissolved cobalt within the US North Atlantic
1007 GEOTRACES transect GA03. Biogeosciences 14, 2715-2739.
1008 Noble, A.E., Saito, M.A., Maiti, K. and Benitez-Nelson, C.R. (2008) Cobalt, manganese, and
1009 iron near the Hawaiian Islands: A potential concentrating mechanism for cobalt within a
1010 cyclonic eddy and implications for the hybrid-type trace metals. Deep-Sea Res. II 55,
1011 1473-1490.
1012 Nozaki, Y., Thomson, J. and Turekian, K.K. (1976) The distribution of 210Pb and 210Po in
1013 the surface waters of the Pacific Ocean. Earth Planet. Sci. Lett. 32, 304-312.
1014 Nozaki, Y., Zhang, J. and Takeda, A. (1997) 2I0Pb and210Po in the equatorial Pacific and the
1015 Bering Sea: the effects of biological productivity and boundary scavenging. Deep-Sea Res. II
1016 44, 2203-2220.
1017 Oguri, K., Kawamura, K., Sakaguchi, A., Toyofuku, T., Kasaya, T., Murayama, M., Fujikura,
1018 K., Glud, R.N. and Kitazato, H. (2013) Hadal disturbance in the Japan Trench induced by the
1019 2011 Tohoku–Oki Earthquake. Sci. Rep. 3, 1915.
1020 Okubo, A., Takeda, S. and Obata, H. (2013) Atmospheric deposition of trace metals to the
1021 western North Pacific Ocean observed at coastal station in Japan. Atmospheric Res. 129-130,
1022 20-32.
1023 Orians, K.J. and Bruland, K.W. (1985) Dissolved aluminium in the central North Pacific.
1024 Nature 316, 427-429.
1025 Orians, K.J. and Bruland, K.W. (1986) The biogeochemistry of aluminum in the Pacific
1026 Ocean. Earth Planet. Sci. Lett. 78, 397-410.

1027 Pinedo-González, P., West, A.J., Tovar-Sanchez, A., Duarte, C.M. and Sañudo-Wilhelmy,
1028 S.A. (2018) Concentration and isotopic composition of dissolved Pb in surface waters of the
1029 modern global ocean. Geochim. Cosmochim. Acta 235, 41-54.
1030 Rahn, K.A. (1976) Silicon and aluminum in atmospheric aerosols: Crust-air fractionation?
1031 Atmospheric Environ. 10, 597-601.
1032 Rigaud, S., Stewart, G., Baskaran, M., Marsan, D. and Church, T. (2015) 210Po and 210Pb
1033 distribution, dissolved-particulate exchange rates, and particulate export along the North
1034 Atlantic US GEOTRACES GA03 section. Deep-Sea Res. II 116, 60-78.
1035 Rolison, J.M., Middag, R., Stirling, C.H., Rijkenberg, M.J.A. and de Baar, H.J.W. (2015)
1036 Zonal distribution of dissolved aluminium in the Mediterranean Sea. Mar. Chem. 177, Part 1,
1037 87-100.
1038 Rudnick, R.L. and Gao, S. (2005) Composition of the continental crust, in: Rudnick, R.L.
1039 (Ed.), The Crust. Elsevier-Pergamon, Oxford, pp. 1-64.
1040 Rusiecka, D., et al. (2018) Anthropogenic Signatures of Lead in the Northeast Atlantic.
1041 Geophys. Res. Lett. 45, 2734-2743.
1042 Saito, M.A. and Moffett, J.W. (2001) Complexation of cobalt by natural organic ligands in
1043 the Sargasso Sea as determined by a new high-sensitivity electrochemical cobalt speciation
1044 method suitable for open ocean work. Mar. Chem. 75, 49-68.
1045 Saito, M.A., et al. (2017) The acceleration of dissolved cobalt's ecological stoichiometry due
1046 to biological uptake, remineralization, and scavenging in the Atlantic Ocean. Biogeosciences
1047 14, 4637-4662.
1048 Schaule, B.K. and Patterson, C.C. (1981) Lead concentrations in the northeast Pacific:
1049 evidence for global anthropogenic perturbations. Earth Planet. Sci. Lett. 54, 97-116.
1050 Schlitzer, R. (2018) Ocean Data View. https://odv.awi.de.
1051 Schlitzer, R., et al. (2018) The GEOTRACES Intermediate Data Product 2017. Chem. Geol.
1052 493, 210-223.
1053 Seyfried Jr, W.E., Seewald, J.S., Berndt, M.E., Ding, K. and Foustoukos, D.I. (2003)
1054 Chemistry of hydrothermal vent fluids from the Main Endeavour Field, northern Juan de Fuca
1055 Ridge: Geochemical controls in the aftermath of June 1999 seismic events. J. Geophys. Res.:
1056 Solid Earth 108, 2429.
1057 Shelley, R.U., Zachhuber, B., Sedwick, P.N., Worsfold, P.J. and Lohan, M.C. (2010)
1058 Determination of total dissolved cobalt in UV-irradiated seawater using flow injection with
1059 chemiluminescence detection. Limnol. Oceanogr.: Methods 8, 352-362.
1060 Slemons, L., Paul, B., Resing, J. and Murray, J.W. (2012) Particulate iron, aluminum, and
1061 manganese in the Pacific equatorial undercurrent and low latitude western boundary current
1062 sources. Mar. Chem. 142-144, 54-67.
1063 Smith, J.N., Rossi, V., Buesseler, K.O., Cullen, J.T., Cornett, J., Nelson, R., Macdonald, A.M.,
1064 Robert, M. and Kellogg, J. (2017) Recent Transport History of Fukushima Radioactivity in
1065 the Northeast Pacific Ocean. Environ. Sci. Technol. 51, 10494-10502.

Sohrin, Y. and Bruland, K.W. (2011) Global status of trace elements in the ocean. Trends Anal. Chem. 30, 1291-1307.
Sunda, W.G. and Huntsman, S.A. (1988) Effect of sunlight on redox cycles of manganese in the southwestern Sargasso Sea. Deep-Sea Res. A 35, 1297-1317.
Talley, L.D., Pickard, G.L., Emery, W.J. and Swift, J.H. (2011) Descriptive Physical Oceanography: An Introduction, 6th ed. Elsevier, Amsterdam.
Thunell, R., Tappa, E., Varela, R., Llano, M., Astor, Y., Muller-Karger, F. and Bohrer, R. (1999) Increased marine sediment suspension and fluxes following an earthquake. Nature 398, 233-236.
van Hulten, M., Middag, R., Dutay, J.C., de Baar, H., Roy-Barman, M., Gehlen, M., Tagliabue, A. and Sterl, A. (2017) Manganese in the west Atlantic Ocean in the context of the first global ocean circulation model of manganese. Biogeosciences 14, 1123-1152.
Von Damm, K.L. and Bischoff, J.L. (1987) Chemistry of hydrothermal solutions from the southern Juan de Fuca Ridge. J. Geophys. Res.: Solid Earth 92, 11334-11346.
Vu, H.T.D. and Sohrin, Y. (2013) Diverse stoichiometry of dissolved trace metals in the Indian Ocean. Sci. Rep. 3, 1745.
Wu, J., Rember, R., Jin, M., Boyle, E.A. and Flegal, A.R. (2010) Isotopic evidence for the source of lead in the North Pacific abyssal water. Geochim. Cosmochim. Acta 74, 4629-4638.
Wuttig, K., et al. (2019) Critical evaluation of a seaFAST system for the analysis of trace metals in marine samples. Talanta 197, 653-668.
Wyrtki, K. and Kilonsky, B. (1984) Mean Water and Current Structure during the Hawaii-to-Tahiti Shuttle Experiment. J. Phys. Oceanogr. 14, 242-254.
Yang, L., et al. (2018) Inter-laboratory study for the certification of trace elements in seawater certified reference materials NASS-7 and CASS-6. Anal. Bioanal. Chem. 410, 4469-4479.
Yasuda, I. (1997) The origin of the North Pacific Intermediate Water. J. Geophys. Res.: Oceans 102, 893-909.
Yasuda, I. (2003) Hydrographic Structure and Variability in the Kuroshio-Oyashio Transition Area. J. Oceanogr. 59, 389-402.
Zheng, L., Minami, T., Takano, S., Minami, H. and Sohrin, Y. (2017) Distribution and stoichiometry of Al, Mn, Fe, Co, Ni, Cu, Zn, Cd, and Pb in seawater around the Juan de Fuca Ridge. J. Oceanogr. 73, 669-685.
Zurbrick, C.M., et al. (2018) Dissolved Pb and Pb isotopes in the North Atlantic from the GEOVIDE transect (GEOTRACES GA-01) and their decadal evolution. Biogeosciences 15, 4995-5014.
Zurbrick, C.M., Gallon, C. and Flegal, A.R. (2017) Historic and Industrial Lead within the Northwest Pacific Ocean Evidenced by Lead Isotopes in Seawater. Environ. Sci. Technol. 51, 1203-1212.

Table 1
Statistical summary of seawater data.

Element	Fraction	*n*				Minimum	Maximum	Median
		Total	> DL	< DL	Questionable and discarded			
Al (nmol/kg)	td	638	610	21	7	< 0.1	59.6	2.16
	d	638	438	76	124	< 0.1	8.63	0.46
	lp	638	436	75	127	< 0.2	56.7	1.13
Mn (nmol/kg)	td	638	633	0	5	0.17	12.3	0.74
	d	638	633	0	5	0.08	8.38	0.52
	lp	638	429	199	10	< 0.1	5.65	0.12
Co (pmol/kg)	td	638	631	0	7	4.5	221	24.1
	d	638	623	3	12	< 0.4	179	20.2
	lp	638	288	332	18	< 4	44.2	< 4
Pb (pmol/kg)	td	638	628	0	10	3.4	89.7	28.5
	d	638	579	0	59	2.0	85.0	28.6
	lp	638	30	545	63	< 4	14.1	< 4

Table

Table 2
Summary of water mass data.

Water mass	Salinity	Potential Temperature [°C]	σ_θ [kg/m^3]	Reference	Al [nmol/kg]			Mn [nmol/kg]			Co [pmol/kg]			Pb [pmol/kg]		
					td	d	lp	td	d	lp	td	d	lp	td	d	lp
Subtropical Mode Water (STMW)			25.2–25.8	Yasuda 2003	0.12–1.3	< 0.1–1.3	< 0.2–1.0	0.54–1.2	0.45–0.79	< 0.1–0.11	15–31	8–25	< 4–13	64–78	62–83	< 4
Central Mode Water (CMW)			26.0–26.7	Yasuda 2003	0.54–4.9	< 0.1–1.6	0.21–1.3	0.27–1.1	0.19–0.95	< 0.1–0.35	28–43	26–39	< 4–10	52–80	56–83	< 4
Okhotsk Sea Mode Water (OSMW)	33.5–33.6	1–2	26.6–27	Yasuda 1997	1.6–6.0	0.21–0.53	1.4–5.5	1.2–2.0	0.51–1.7	0.27–0.91	48–75	50–72	< 4–7	31–52	30–51	< 4
North Pacific Intermediate Water (NPIW)	33.8–34.1		26.4–27.2, averaging 26.8	Dickson et al. 2000, Bostock et al. 2010	1.0–6.8	0.18–1.1	0.63–6.1	0.32–1.1	0.22–0.74	< 0.1–0.37	34–47	30–43	< 4–9	44–71	41–63	< 4–6
Equatorial Pacific Intermediate Water (EqPIW)	34.5–34.6		27.3	Bostock et al. 2010	1.1–2.5	0.87–1.9	< 0.2–1.6	0.32–0.43	0.22–0.36	< 0.1–0.14	32–39	30–38	< 4	12–25	12–28	< 4
Upper Circumpolar Deep Water (UCDW)	34.6	2.5	27.6	Talley et al. 2012	1.2–3.0	0.73–1.6	< 0.2–1.2	0.22–0.38	0.17–0.23	< 0.1–0.16	21–30	17–29	< 4	7–12	9–14	< 4
Pacific Deep Water (PDW)	34.7	1.1–1.2	27.7	Talley et al. 2011	0.88–4.5	< 0.1–0.86	0.63–3.7	0.19–0.82	0.13–0.66	< 0.1–0.33	14–26	13–23	< 4–6	9–31	6–32	< 4–6
Lower Circumpolar Deep Water (LCDW)	34.7	1–2	27.8	Talley et al. 2013	1.5–40	0.36–4.1	0.60–37	0.16–5.7	0.08–1.3	< 0.1–4.4	12–32	8–20	< 4–20	3–16	3–16	< 4–6

Figure1

Click here to download high resolution image

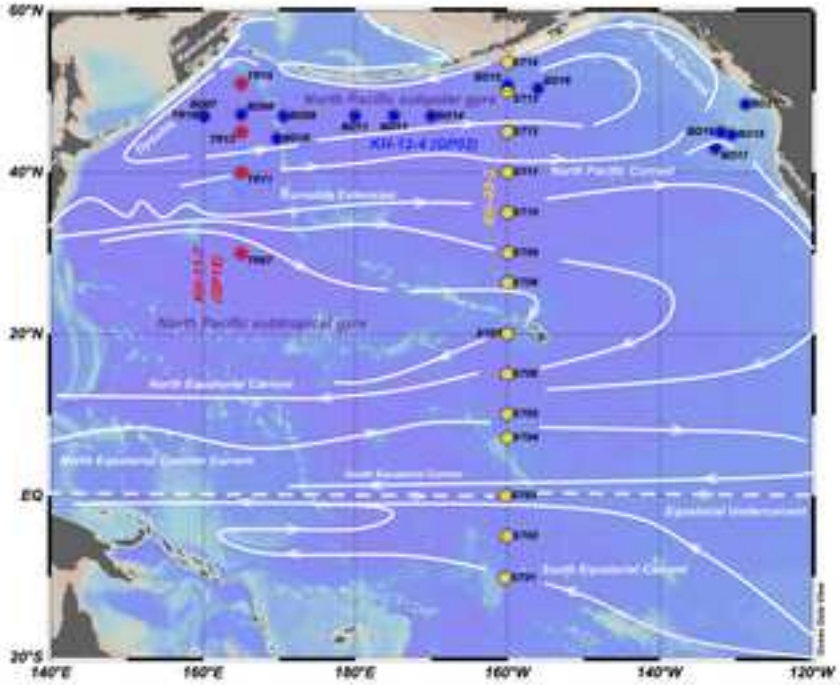

Figure 1

Figure2

Click here to download high resolution image

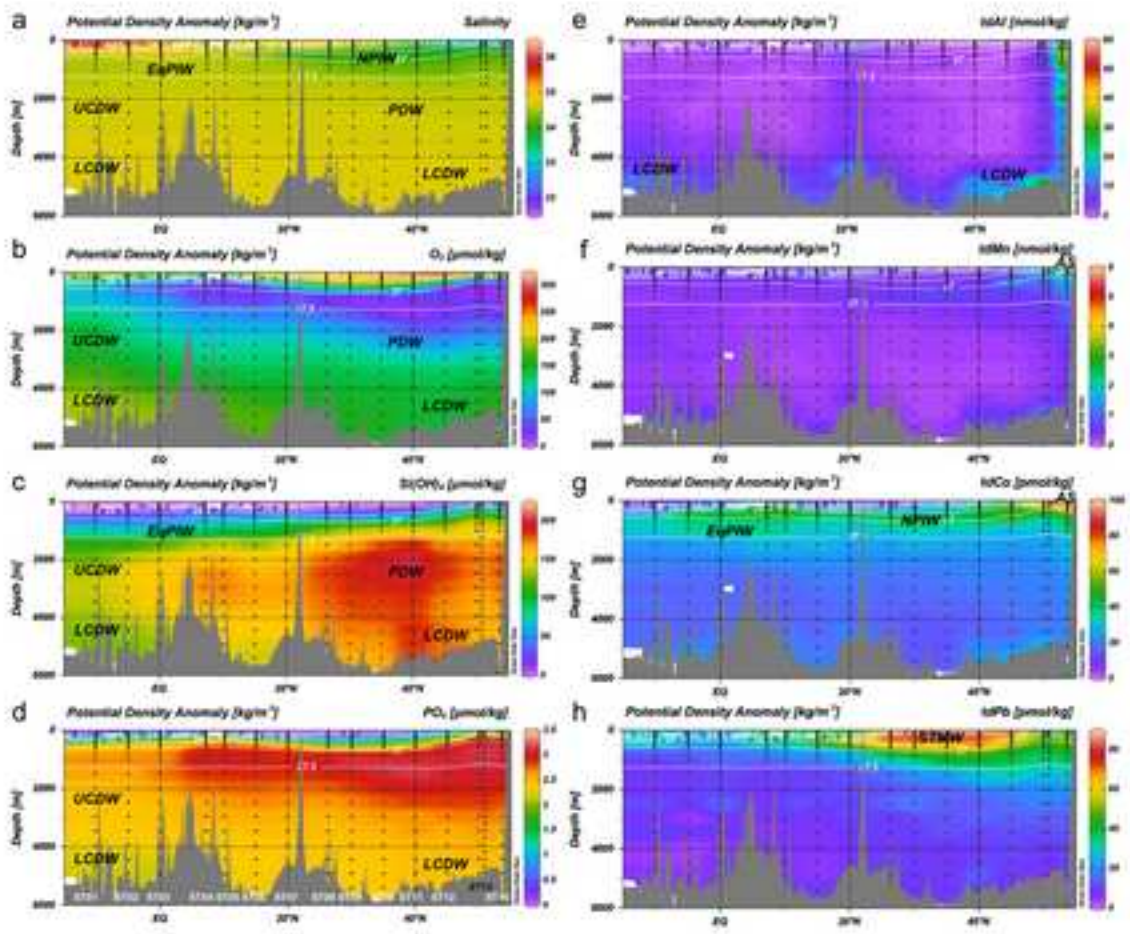

Figure 2

Figure3

Click here to download high resolution image

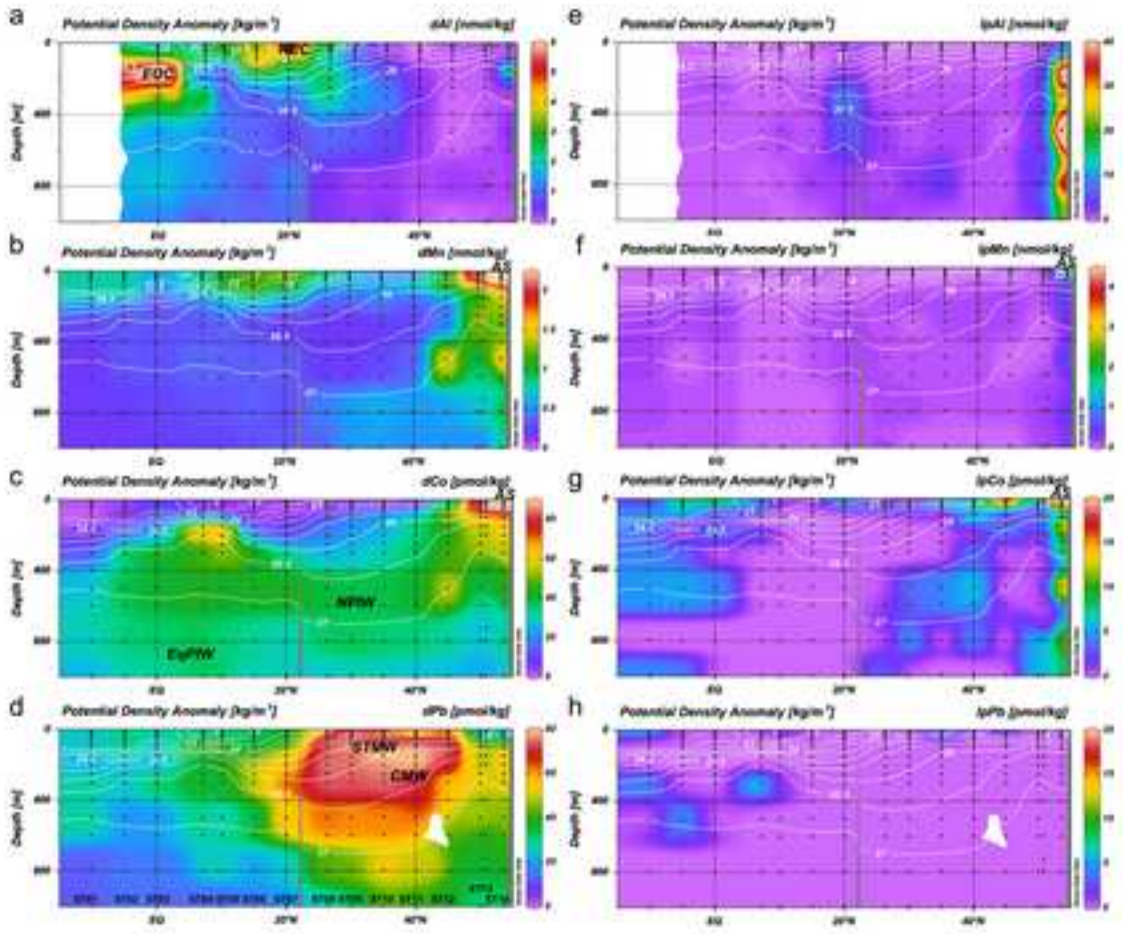

Figure 3

Figure4

Click here to download high resolution image

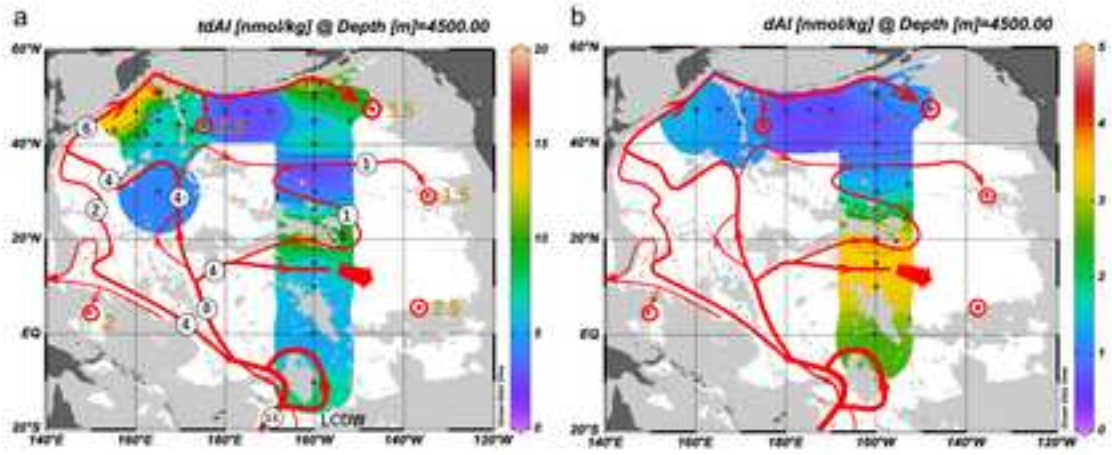

Figure 4

Figure5

Click here to download high resolution image

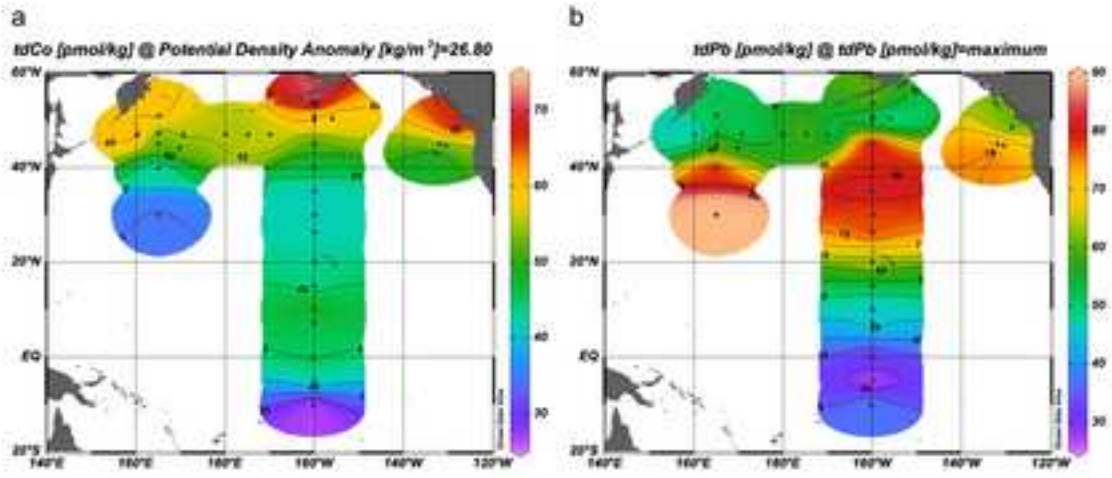

Figure 5

Figure6

Click here to download high resolution image

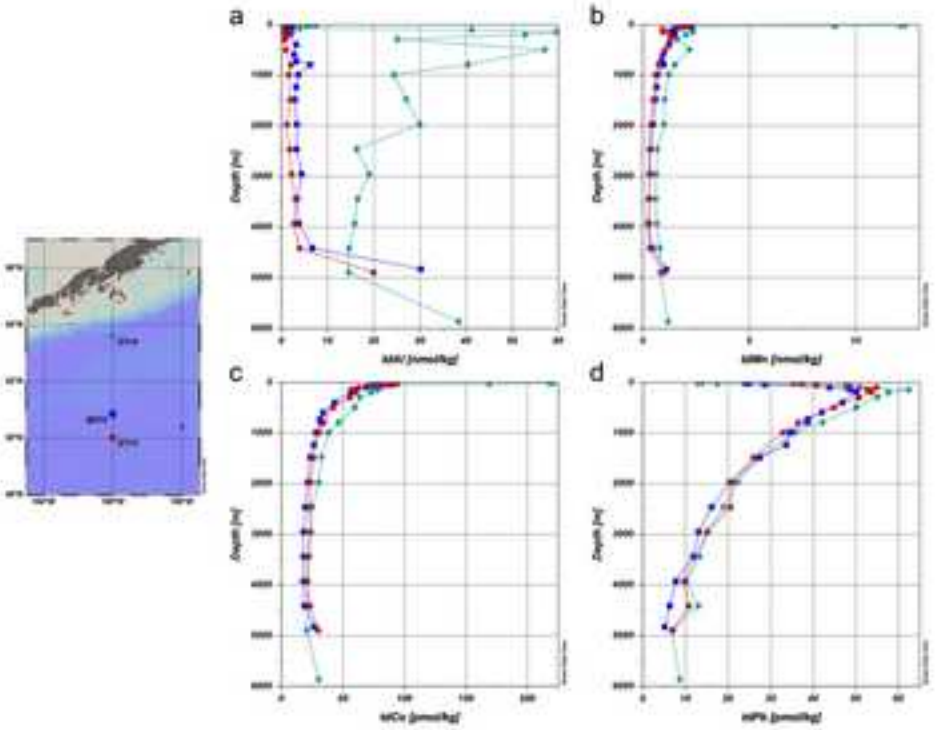

Figure 6

Figure7

Click here to download high resolution image

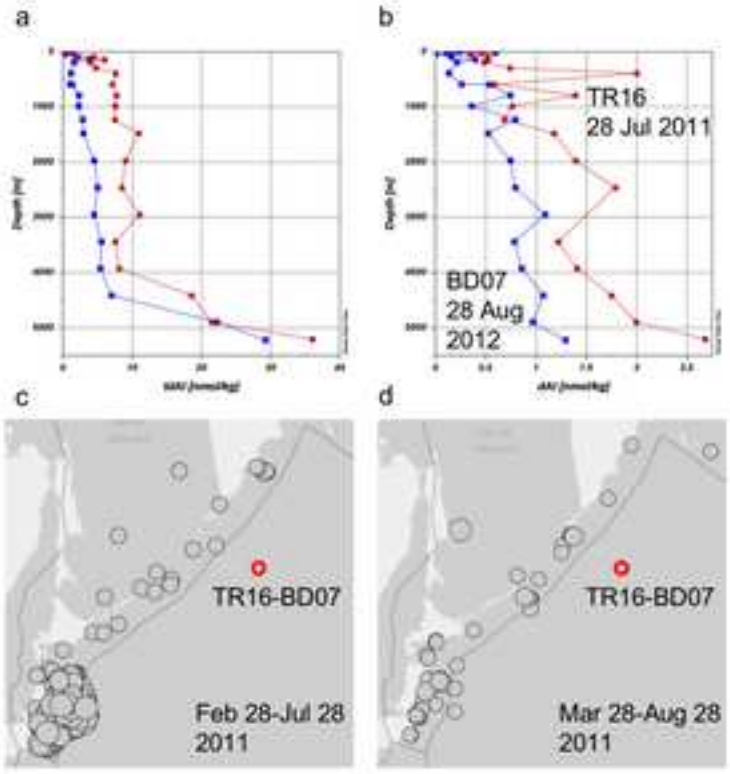

Figure 7

Figure8

Click here to download high resolution image

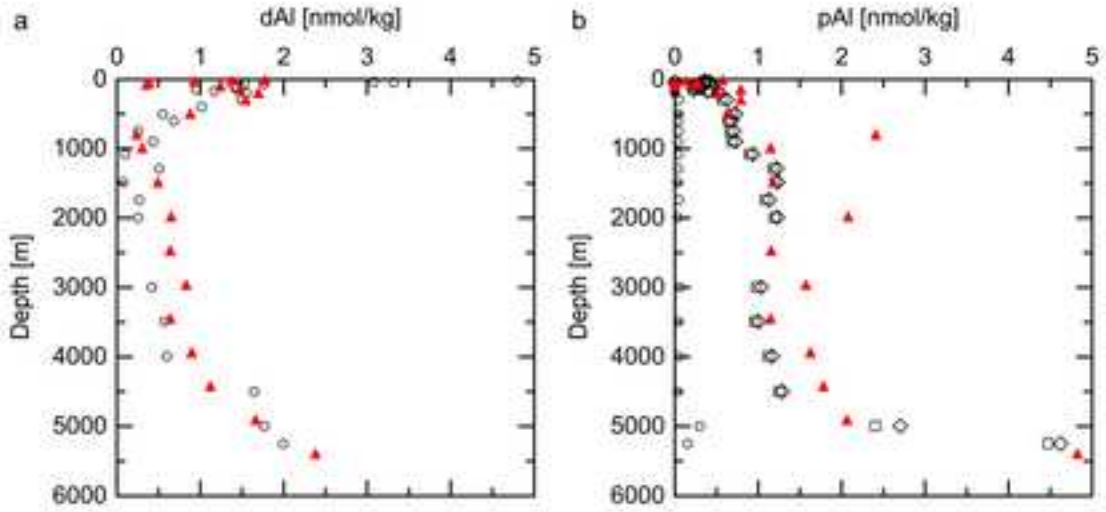

Figure 8

Figure9

Click here to download high resolution image

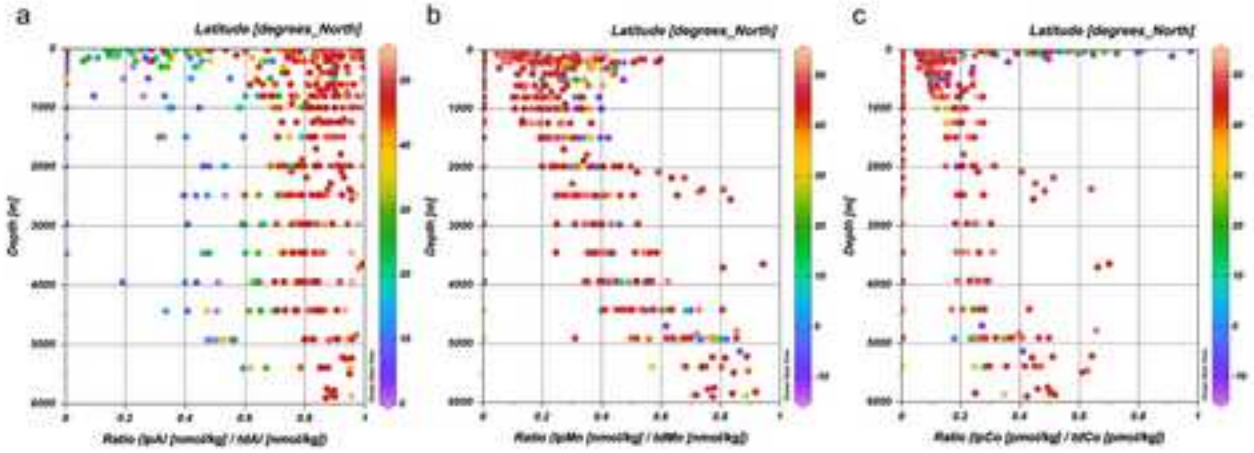

Figure 9

Figure10
Click here to download high resolution image

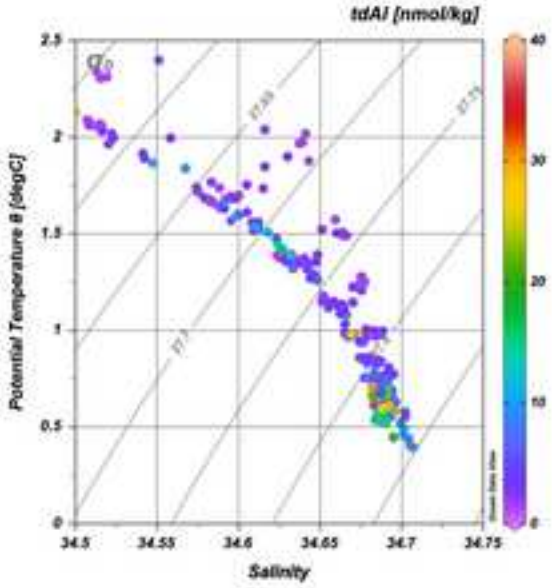

Figure 10

Figure11

Click here to download high resolution image

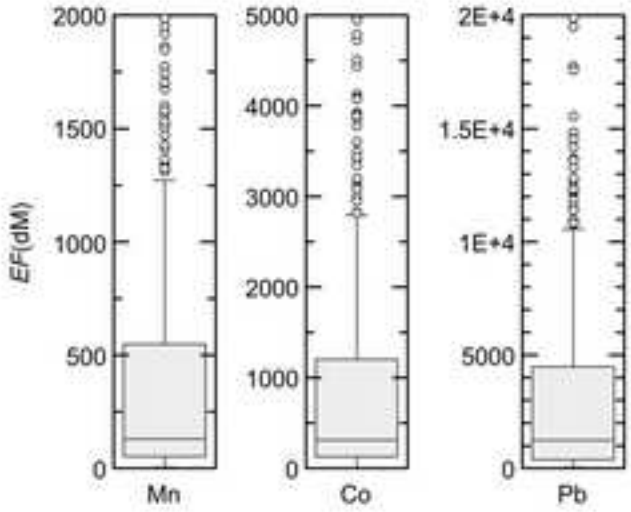

Figure 11

Figure12
Click here to download high resolution image

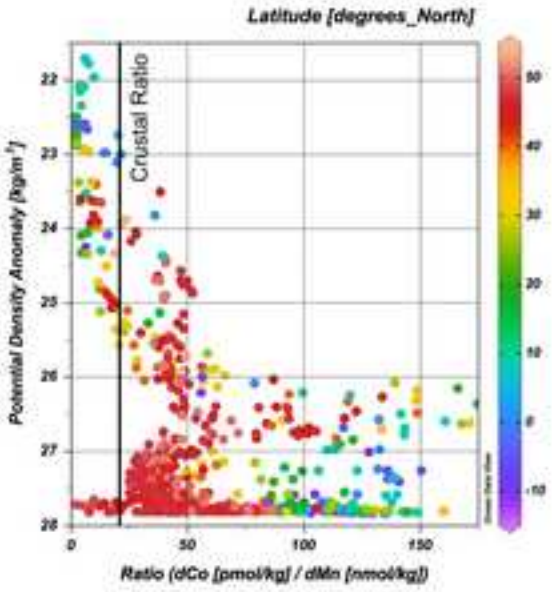

Figure 12

Figure13
Click here to download high resolution image

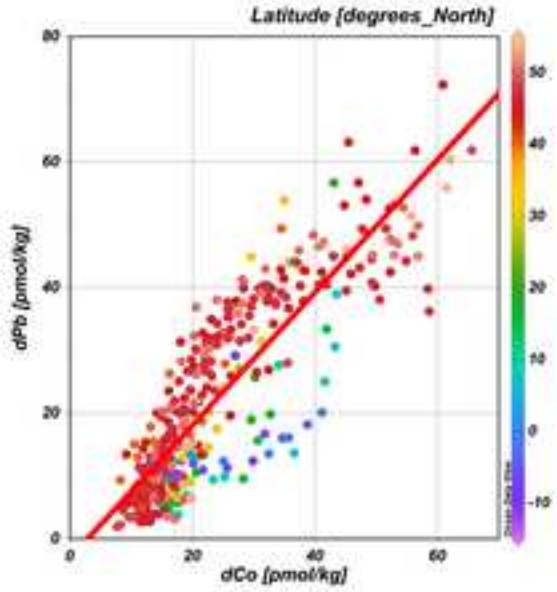

Figure 13

Supplementary Tables

Click here to download Appendix: SupplementaryTables.xlsx

Supplementary Figure Captions

Click here to download Appendix: SupFigCaps.docx

Supplementary Figures

Click here to download Appendix: SupplementaryFigs.pptx